TÉCNICO LISBOA

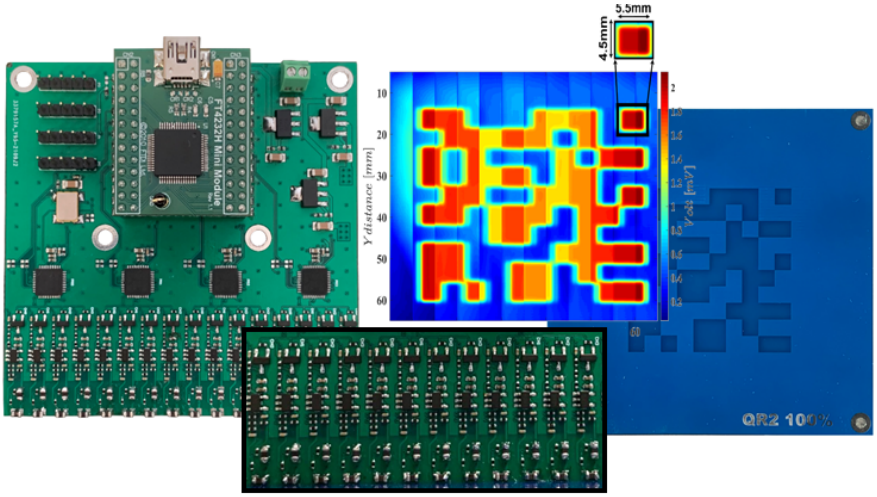

Eddy Current Array Probe for Metal Additive Manufacturing Imaging

André Barrancos Oliveira

Thesis to obtain the Master of Science Degree in

Electronics Engineering

Supervisor: Prof. Luís Filipe Soldado Granadeiro Rosado

Examination Committee

Chairperson: Prof. Paulo Ferreira Godinho Flores
Supervisor: Prof. Luís Filipe Soldado Granadeiro Rosado
Member of the Committee: Prof. Fernando Manuel Tim Tim Janeiro

November 2021

Declaration

I declare that this document is an original work of my own authorship and that it fulfills all the requirements of the Code of Conduct and Good Practices of the Universidade de Lisboa.

Acknowledgments

As I close one of the most symbolic chapters of my life, it wouldn't be appropriate without greeting and thanking every soul that stood by my side.

First of all, I would like to thank to the Profesor Luis Rosado, who shared all his knowledge to finish my thesis. It was a pleasure and a great opportunity to work with him during this year.

Secondly, I would like to mention my colleagues, especially those that were with me, concluding the thesis. My thankfulness to Hugo Cunha, Markiyan Pyekh, Pedro Coutinho and Sara Soares for the hours of hard work and companionship. Without them, completing the thesis would be way more challenging.

I also would like to thank my family, specifically my parents Laurindo Oliveira and Filomena Barrancos, who gave me this opportunity and all the support I needed. Also a special thanks to my brother Miguel Oliveira and cousin Beatriz Oliveira for all the support during these months.

I also want to thank the Instituto de Telecomunicações for the conditions and materials provided for the completion of the dissertation.

Last but not least, to all my friends and remaining family members that helped me grow as a person and were always there for me during the good and bad times in my life.

To each and every one of you – Thank you.

Abstract

Metal Additive Manufacturing has been developing over the years, and nowadays is becoming a promising manufacturing technology. Thanks to metal additive manufacturing, more complex metal parts can be easily produced using innovative technologies like Metal Powder Bed Fusion, which employs laser energy to melt and consolidate stacked layers from a base metal powder. However, in the metal additive manufacturing industry, the manufactured pieces' defects prevent the industry from widespread adoption by the mainstream industry [1], so to assure that this technique becomes more used, high-quality standards are essential.

Eddy current testing, a non-destructive testing technique, is based on the generation and analysis of induced electrical currents in the test material [2]. It is a widely used technique in the metal industry to evaluate the metal's properties without causing any damage. This work presents the development of an eddy current array probe and readout circuits, which will allow online detection of defects layer by layer on metal powder bed fusion, providing high spatial resolution, spatial coverage and speed. This project objective is to develop a scalable architecture enabling a cost-effective modular and extendable probe with 16 sensing coils.

Initially, some coils were tested to decide which would be the best sensing elements for the final array probe. Also, some initial PCB tests were made to develop an eddy current system with as minimal hardware as possible. The final system is able to process the data at high speeds and send the information to a computer to make the imaging of the test material in real-time.

The array probe has the following specifications: Total size of 80x80 mm; Coils pitch of 5 mm; Total acquisition rate of 20 kSamples/s; Acquisition rate per channel of 5 kSample/s; Demodulation and stimulation frequency up to 1.5 MHz; Internal clock system of the MSP430s of 24 MHz; External oscillator of 24 MHz; Supply voltage from 0 V to 12 V; Total power consumption of 3 W and a total cost of 40 €.

Keywords

Metal Additive Manufacturing, Non-Destructive Testing, Eddy Currents Testing, High Resolution, Minimalist Signal Demodulator.

Resumo

O fabrico aditivo de peças metálicas tem vindo a desenvolver-se ao longo dos anos, e hoje em dia está a tornar-se uma tecnologia de fabrico promissora. Com esta tecnologia, peças metálicas complexas podem ser facilmente produzidas utilizando tecnologias inovadoras como a *Metal Powder Bed Fusion*, que emprega energia laser para fundir e consolidar camadas sucessivas a partir de um pó metálico. No entanto, na indústria de fabrico de aditivos metálicos, os defeitos das peças fabricadas impedem a adopção generalizada pela indústria [1], de modo a assegurar que esta técnica se torne mais utilizada, normas de alta qualidade são essenciais.

O ensaio por correntes induzidas é uma técnica de ensaio não destrutiva, baseada na geração e análise de correntes elétricas induzidas no material de ensaio [2]. É uma técnica amplamente utilizada na indústria metalúrgica para avaliar as propriedades de peças metálicas sem causar qualquer dano ao mesmo. Este trabalho visa desenvolver uma sonda matricial de correntes induzidas e circuitos de leitura, que permitirão a detecção de defeitos camada por camada ao longo da produção das peças metálicas. A sonda será composta por circuitos de leitura que proporcionem alta resolução e cobertura espacial e velocidade. Neste projecto foi desenvilvido uma sonda matricial com arquitetura escalável em termos de custo e área, com 16 bobines.

Inicialmente testou-se várias bobines para ajudar a decidir quais seriam as bobines que seriam utilizadas para a sonda matricial final. Também foram desenvolvidas umas sondas preliminares de modo a fazer vários testes de hardware e firmware, de modo a optimizar ao máximo o hardware e os custos da sonda final. O sistema final processa a informação a altas velocidades e a imagiologia das peças em tempo real.

A sonda matricial tem as seguintes especificações: Tamanho 80x80 mm; Distância entre bobines 5 mm; Ritmo de aquisição total 20 kSamples/s; Ritmo de aquisição por canal 5 kSamples/s; Frequência de demodulação/estimulação até 1.5MHz; Relógio interno dos MSP430s 24 MHz; Oscilador externo com frequência 24 MHz; Tensão de entrada 0 V aos 12 V; Consumo total 3 W e custo total de 40€.

Palavras Chave

Fabrico Aditivo de Peças Metálicas, Ensaio Não Destrutivo, Teste de Correntes Induzidas, Alta Resolução, Demodulador de Sinal Minimalista.

Contents

List of Figures

List of Tables

Acronyms

AC	Alternate Current
ADC	Analog-to-Digital Converter
AM	Additive Manufacturing
BJ	Binder Jetting
CMRR	Common-mode Rejection Ratio
CNC	Computer Numerical Control
DAC	Digital to Analog Converter
DC	Direct Current
DDS	Direct Digital Synthesizer
DED	Direct Energy Deposition
ECT	Eddy Currents Testing
GBW	gain-Bandwidth Product
GUI	Graphical User Interface
I/O	Input/Output
ID	Inside Diameter
MAM	Metal Additive Manufacturing
NDT	Non-Destructive Testing
Op-amp	Operational Amplifier
OD	Outside Diameter
PBF	Powder Bed Fusion
PCB	Printed Circuit Board
PGA	Programmable Gain Amplifier

PEC	Pulsed Eddy Currents
PWM	Pulse Width Modulation
QC	Quality Control
SAC	Smart Analog Combo
SL	Sheet Lamination
SR	Slew-Rate
UART	Universal Asynchronous Receiver-Transmitter
USB	Universal Serial Bus

1

Introduction

Contents

1.1 Purpose and Motivation

Metal Additive Manufacturing (MAM) is a 3D manufacturing process, where the fabrication of a 3D object is accomplished by joining layers of metal, layer by layer. Nowadays, more and more companies rely on this type of technology to create prototypes and even to create a final product. This type of manufacturing has some advantages like the ability to produce sophisticated objects in a wide range of materials and reduced production setup times compared to other forms of metal manufacturing processes.

There are a lot of innovative technologies used in the MAM industry, where the most used are Binder Jetting (BJ), Sheet Lamination (SL), Direct Energy Deposition (DED) and Powder Bed Fusion (PBF). In this work, the focus will be in the PBF technology, which is a type of manufacturing process used to produce metal addictive parts, where the laser energy is used to melt and consolidate stacked layers from a base metal powder.

In order to achieve high quality produced parts it is essential to have high standards of Quality Control (QC), and the ability to detect as much as possible defects while the metal additive parts are being produced. Non-Destructive Testing (NDT) techniques allow to analyze materials without damaging them while detecting any defects or flaws. That's why NDT plays an essential role on the QC that currently exists in the MAM industry, since it's vital to evaluate the integrity of the produced parts, while tests are made during manufacturing.

In-situ monitoring of PBF produced parts, nowadays rely on optical sensors, infrared cameras, thermal cameras and laser-assisted ultrasound tests. These testing technologies have some advantages like being fine-tuned over the years, but they require lots of computational power and most systems do not sample signals at high rates and interpret them immediately (in real-time) [17].

This work aims to use a different approach for the QC of PBF parts. Eddy Currents Testing (ECT) is a popular choice for the characterization of conductive parts within the NDT methods. Eddy Currents probes can inspect ferromagnetic and non-ferromagnetic materials, with very accurate and high-speed results while being cost-effective. But the main advantage for the MAM industry is that ECT can measure the effective consolidation between successive layers of the test piece and, that's why ECT can be an excellent alternative to what is currently used in the MAM industry.

1.2 Goals and Challenges

The main purpose of this project is to develop a wide ECT array probe and readout circuits providing high spatial resolution, spatial coverage and speed. As such, the goals for this project are:

- Study different type of sensitive elements to be employed on the array probes together with the possibility of using industrial electronics discrete components for its physical implementation;
- Evaluate the several possibilities concerning probe excitation and the sensing elements readout to obtain the best ratio between fast sensor reading and best resolution;
- Develop a frontend to enable individual readout from each sensing element.
- Design and prototype the probe hardware and perform validation tests;

The main challenges will be to develop a circuit that can have a high-speed readout from the many sensing elements, and guarantee a scalable electronic in terms of area and cost to implement arrays with 16 sensing elements.

1.3 Document Organization

This document is organized into four chapters, as follows:

- Chapter 2 is the state of the art. This chapter covers an introduction about NDT, the theory about eddy currents and ECT, and finally an overview of MAM. The purpose of this chapter is to give the reader an essential background to understand the developed work.
- Chapter 3 presents the initial setup and developed Printed Circuit Board (PCB)s to test various coils to help decide which are the best sensing elements for the final array probe.
- In Chapter 4 an one channel PCB in order to make the necessary changes to make a minimal system in terms of hardware and firmware. After that, the final array probe is presented and the Labview program used to acquire the data. The chapter concludes with the presentation of the results.
- Chapter 5 presents a thesis overview, a conclusion about the results achieved and future work suggestions.

2

State of the art

Contents

2.1 Eddy Current Testing

NDT is a broad group of analysis techniques used to evaluate if an object/material has any defects or discontinuities without damaging it. NDT has a broad use from detecting faults on metal surfaces to inspect defects in art pieces.

ECT is one of the various methods in the NDT industry and can be used in metallic materials to detect superficial and buried defects. It's essential to know the type of surfaces analyzed so that the most suited probe design can be achieved to get the best performance. So in this section, it's covered an overview of ECT and an insight of ECT probes.

2.1.1 Eddy Currents Phenomenon

Eddy currents phenomenon occurs when a conductive material is close to a varying magnetic field. An electrical voltage is induced in the material, which generates the eddy currents, perpendicular to the magnetic field source and perpendicular to the vector of the magnetic induction, as an electrical current in a closed loop.

In the eddy current probes, a coil generates an alternating magnetic field that induces the eddy currents in the test material [3]. The generated eddy currents magnitude is proportional to the magnetic flux's change rate, but it's inversely proportional to the material's resistivity [18]. The measurement system senses the changes of the magnetic field generated by the eddy currents, through the same coil or another sensing coil. The voltage output of the measurement system depends on the eddy current's magnetic field variation, which is affected by the distance of the probe to the target material, or if the testing material is different or if the material under test has any discontinuities. In Fig. 2.1, depicts how eddy currents can be induced by a coil when an Alternate Current (AC) current is flowing.

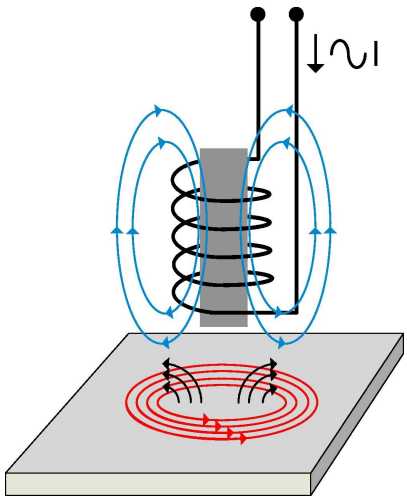

Figure 2.1: Eddy currents being induced by a coil. Taken from [3].

Eddy current phenomenon can be explained by the Ampère–Maxwell [19] and Faraday's equations [20]. The first equation is given by

$$\oint \vec{B}\, d\vec{s} = \mu_0 I_\mathrm{c} + \mu_0 \varepsilon_0 \frac{\partial \Phi_E}{\partial t}, \tag{2.1}$$

where $\vec{B}$ $[T]$ is the magnetic field, I_c $[A]$ is the current passing through the coil, μ_o $\left[Hm^{-1}\right]$ is the magnetic permeability of free space, ε_0 $\left[Fm^{-1}\right]$ is the electric permittivity of free space, and $\frac{\partial \Phi_E}{\partial t}$ $[Vms^{-1}]$ is the rate of change of the electric flux.

If the frequency of the current is low enough, the displacement current term of 2.1 can be discarded, resulting in

$$\oint \vec{B}\, d\vec{s} = \mu_0 I_\mathrm{c}. \tag{2.2}$$

Knowing the magnetic field generated by the coil in 2.2, it's possible to get the magnetic flux $[Wb]$ passing through the metal represented in Fig. 2.1. The magnetic flux is

$$\Phi_{\vec{B}} = \int \vec{B}\, dA, \tag{2.3}$$

using the magnetic flux obtained in 2.3 and using Faraday's law of induction

$$\oint \vec{E}\, dl = -\frac{\partial \Phi_B}{\partial t}, \tag{2.4}$$

it's possible to calculate the induced electromotive force $[V]$ that generates the eddy currents, represented in red in Fig. 2.1.

2.1.2 Skin effect

The eddy currents are distributed along the test material. The current density decreases in the material's depth being tested, so the current density will be higher at the surface and lower while moving deeper into the material. The amplitude of the current density induced by an electromagnetic wave, perpendicularly incident to a conductive material [21], decreases at a depth x according to

$$J(x) = J_0 e^{-x\sqrt{\pi f \mu_0 \mu_r \sigma}}, \tag{2.5}$$

where J_0 $[Am^{-2}]$ is the maximum current density when $x = 0$, f $[Hz]$ is the frequency of the magnetic field source, μ_r $\left[Hm^{-1}\right]$ is the test material's relative magnetic permeability, and σ $[Sm]$ is the test material's electric conductivity [22].

In Fig. 2.2, it's shown how the density of eddy currents changes along the test material when it's

used higher or lower frequencies.

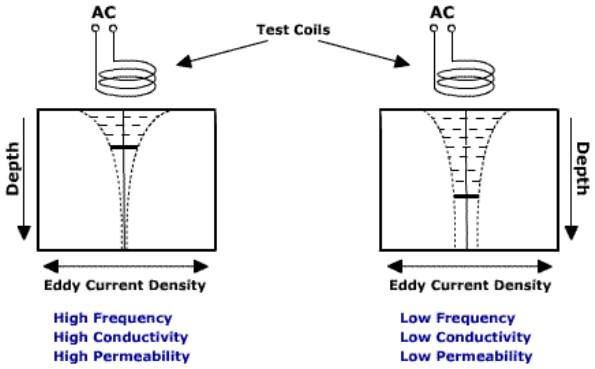

Figure 2.2: Eddy currents density through the test material. Taken from [4].

The depth of penetration is how far the eddy currents penetrate the test material until the current density decreases $1/e \approx 37\ \%$ [22] from the initial density at the material's surface. From equation 2.5, it's possible to get the depth of penetration. Knowing that $\frac{J(x)}{J_0} = \frac{1}{e}$ results in

$$\frac{1}{e} = e^{-x\sqrt{\pi f \mu_0 \mu_r \sigma}}, \tag{2.6}$$

which by putting x in evidence gives the depth of penetration

$$x = \delta = \frac{1}{\sqrt{\pi f \mu_0 \mu_r \sigma}}. \tag{2.7}$$

By reducing the frequency, it is possible to get a higher depth of penetration, but the current density will be less at the surface. The Table 2.1 and Fig. 2.3 shows how far eddy currents penetrate a test material, when the frequency is changing, in two non-ferromagnetic materials Copper ($\mu_r = 1$ and $\sigma = 5.96 \times 10^7$) and Aluminum ($\mu_r = 1$ and $\sigma = 3.5 \times 10^7$), and one ferromagnetic material Stainless Steel ($\mu_r = 1000$ and $\sigma = 1.45 \times 10^6$).

Table 2.1: Depth of penetration in copper, aluminium and stainless steel.

Frequency	Depth of penetration $[\mu m]$		
	Copper	Aluminum	Stainless Steel
50 Hz	9296.27	12030.84	1866.68
60 Hz	8416.33	10982.61	1704.04
10 kHz	651.92	850.71	131.99
100 kHz	206.16	269.02	41.74
1 MHz	65.19	85.07	13.20
10 MHz	20.62	26.90	4.17

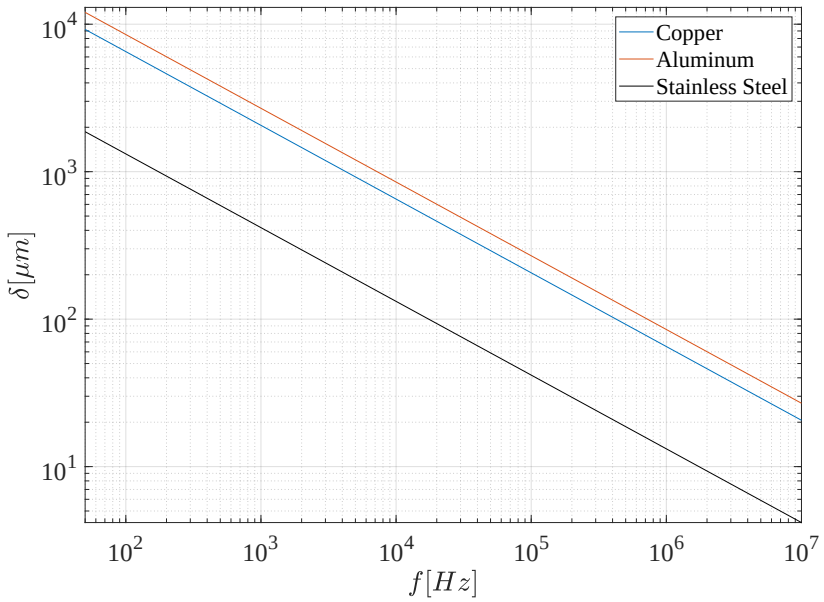

Figure 2.3: Graph for the depth of penetration in copper, aluminium and stainless steel.

2.1.3 Impedance Plane

The induced eddy currents are mainly affected by electrical conductivity or magnetic permeability, test frequency and the distance between the coil and test material, also known as lift-off [2]. Measuring the coil impedance provides useful information about the material under testing, so impedance planes are useful to make an easier interpretation of the results obtained. Fig. 2.4 shows how a coil impedance changes in the presence of different perturbations and types of materials.

In Fig. 2.4 it is observed that when the coil is close to a ferromagnetic or non-ferromagnetic the real component of the impedance increases due to eddy currents generation. This occurs because it takes energy away from the coil.

On non-ferromagnetic materials, the imaginary part of the impedance decreases because the eddy currents magnetic field opposes to the coil's magnetic field, resulting in a weaker magnetic field sensed by the coil. In the presence of a crack, fewer eddy currents will be induced on the test material, and so the impedance imaginary part will increase, and the real part will decrease.

On ferromagnetic materials, because of their higher magnetic permeability, it will concentrate the coil's magnetic field on the material. Consequently overshadowing the eddy currents magnetic field, which makes the impedance reactance increase. In the presence of a crack, the coil's impedance behaviour will be the same as a non-ferromagnetic material.

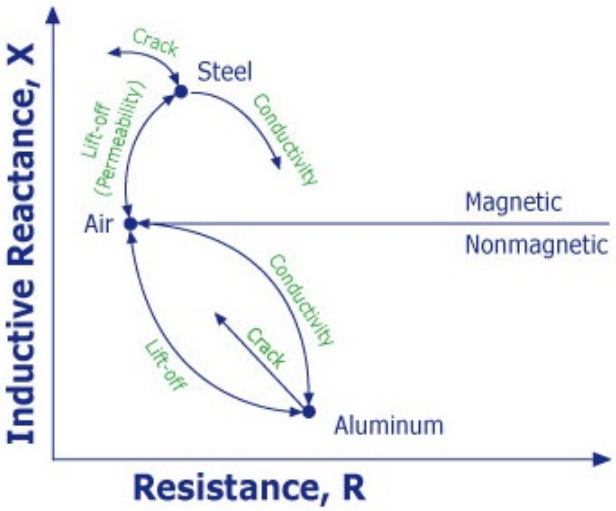

Figure 2.4: Impedance plane diagram. Taken from [5].

2.1.4 Types of probes

Represented in Fig. 2.5, absolute probes use one coil that generates the eddy currents and sense the eddy currents' magnetic field variations. This type of probes can be used in flaw detection and thickness, lift-off, and conductivity measurements. The main disadvantages of these probes is the strong baseline signal when compared to that caused by a defect, so it's crucial to minimize this baseline [23] subtracting the signal from a second reference coil that is not in contact with the inspected material as shown in Fig. 2.5.

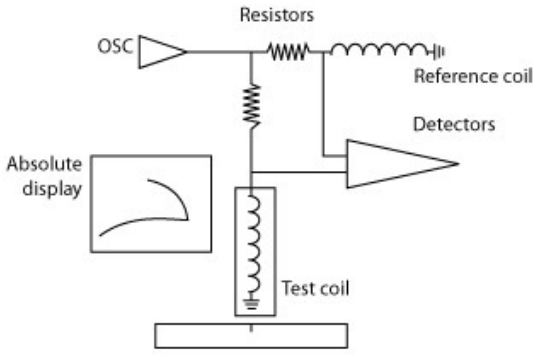

Figure 2.5: Absolute probe electric circuit. Taken from [6].

Represented in Fig. 2.6, differential probes use two active coils that generate a differential output. These probes only detect a differential signal when one of the coils is over a defect, and the other coil is over the material with no flaw. These probes have the advantage of being very sensitive while detecting faults, but their signals can sometimes be hard to interpret [23].

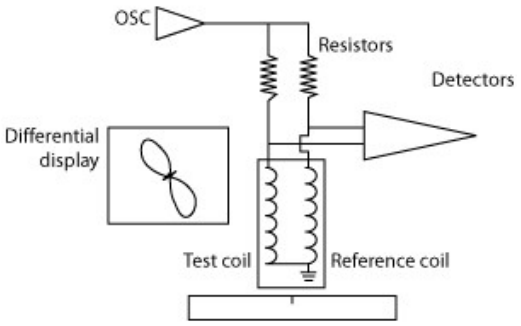

Figure 2.6: Differential probe electric circuit. Taken from [6].

Represented in Fig. 2.7, reflection probes have two coils, where one coil generates the eddy currents and the other senses the magnetic field variations induced by the eddy currents. This type of probes have the advantage that each coil can be optimized in its way. This means that the coil generating the eddy currents can be fine-tuned to produce a stronger and uniform magnetic field, while the sensing coil can be smaller and more sensitive to smaller defects [23].

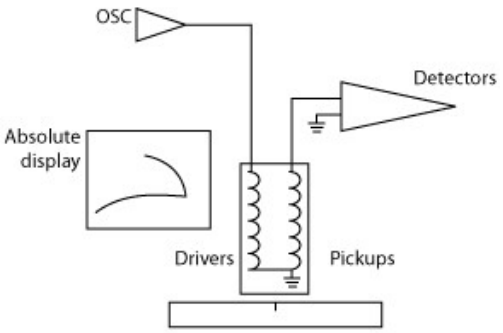

Figure 2.7: Reflection probe electric circuit. Taken from [6].

Represented in Fig. 2.8, hybrid probes usually have a driver coil to induce the eddy currents and a different magnetic sensing element, like Giant Magneto Resistance (GMR) sensor, to detect the magnetic field variations.

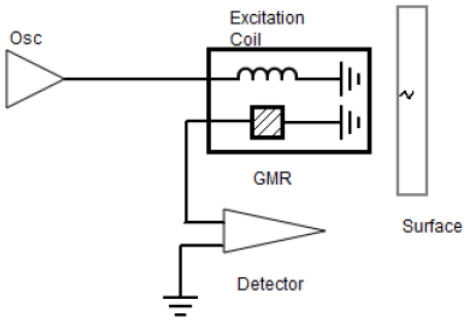

Figure 2.8: Hybrid probe electric circuit. Taken from [7].

2.1.5 Probes Configuration

Represented in Fig. 2.9, surface probes usually have an enclosed coil in a protective cover, where the size of the coil and the cover depends on the expected application. They are usually probes designed to have the coil axis perpendicular to the test surface. These type of probes are usually used to inspect welding joints, surface parts, gears and etc... [11].

Figure 2.9: Surface probes. Taken from [8].

Represented in Fig. 2.10, bolt hole probes have a surface coil inside a shell that has the same diameter as the hole that wants to be inspected, then the probe is inserted inside the hole, and the scanner rotates the probe inside the hole [11].

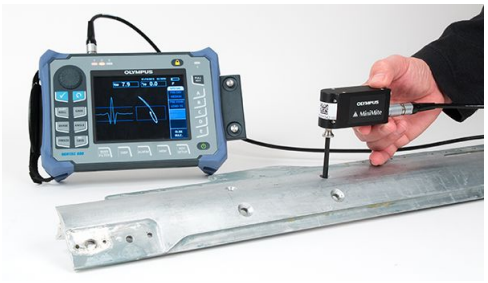

Figure 2.10: Bolt hole probe. Taken from [9].

Represented in Fig. 2.11, Inside Diameter (ID) probes are normally used to inspect pipes. The ID probes have a shell that keeps the probe centered, and the distance of the coil to the test surface always the same. Most of the time, the coils are around the probe, so the probe inspects the area around it [11].

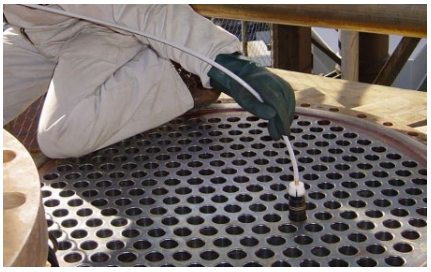

Figure 2.11: ID probes. Taken from [10].

Represented in Fig. 2.12, Outside Diameter (OD) probes are similar to ID probes, but the probe encircles the test material to inspect the material's exterior. These probes are typically used to inspect metal bars and cylinders [11].

Figure 2.12: OD probe. Taken from [11].

Represented in Fig. 2.13, array probes provide the ability to drive and sense multiple eddy current coils, which are placed side by side in the same probe assembly. This type of probes allows to cover larger areas, 3D imaging of the cover area and inspect complex shapes [24].

Figure 2.13: Array probe. Taken from [12].

2.1.6 Stimulus

In order to obtain the maximum information about a defect is essential to know what is the best stimulus to use. In this chapter, different signals with different spectral composition will be covered in order to obtain the maximum information about the material under test, like the present defect's depth and width.

2.1.6.A Conventional ECT stimulus

Conventional ECT stimulus employ a pure sinusoidal excitation, which makes it unable to detect defects at the surface and sub-surface of the testing material at the same time. Thus, the user would have to repeat the testing sweep to analyze the defect's depth with more accuracy. This would lead to data interpretation problems since the data's spatial reference of the several sweeps wouldn't be the same, and inefficient in time because would have to sweep through all the frequencies [25].

2.1.6.B Multi-Frequency ECT stimulus

In order to overcome the spatial reference and time inefficiency problems, Multi-Frequency ECT stimulus can be an alternative. Multi-Frequency sequential excitation is a possible implementation for multi-frequency ECT. Sinusoidal chirp waveforms are sometimes used, and in this case, the frequency is changed with a change rate, defined by the user, in time. Another alternative, to time multiplexing, is frequency multiplexing, where several sinusoids signals are added into a single waveform [25]. These multi-frequency ECT stimulus have the advantage to provide information at different depths [26].

2.1.6.C PEC stimulus

When compared to conventional ECT, Pulsed Eddy Currents (PEC) have some advantages like higher robustness to interferences, detect defects in greater depth, and richer information about the defects [27]. Also, when compared to sinusoidal excitation it can minimize power consumption [28]. Square and sawtooth stimulus with just one signal excitation can scan the test piece defect in depth. However, the amplitude spectrum of these signals decays $1/n^2$, which means that for higher frequencies, the amplitude of the signals might not be distinguishable from noise. Fig.2.14 a) and b) shows the square and sawtooth waveforms and their signal spectrums, respectively. From Fig. 2.14 a), it can be observed that the square signal spectrum components have higher energy, compared to the sawtooth signal spectrum components. On the other hand, the sawtooth signal spectrum contains all the multiple frequencies of the fundamental frequency [2], while the square signal spectrum only includes the odd components of the fundamental frequency.

One way to have higher energy components in the higher frequencies in the signal spectrum is by using a square stimulus with a duty cycle lower than $50\ \%$. In Fig. 2.14 c) is shown a square signal with a duty cycle of $25\ \%$, and it can be observed that with smaller duty cycles the signal spectrum has lower amplitudes components for lower frequencies, but for higher frequencies, it has higher energy. This way, shorter duty cycles allows for more detailed inspections closer to the material's surface.

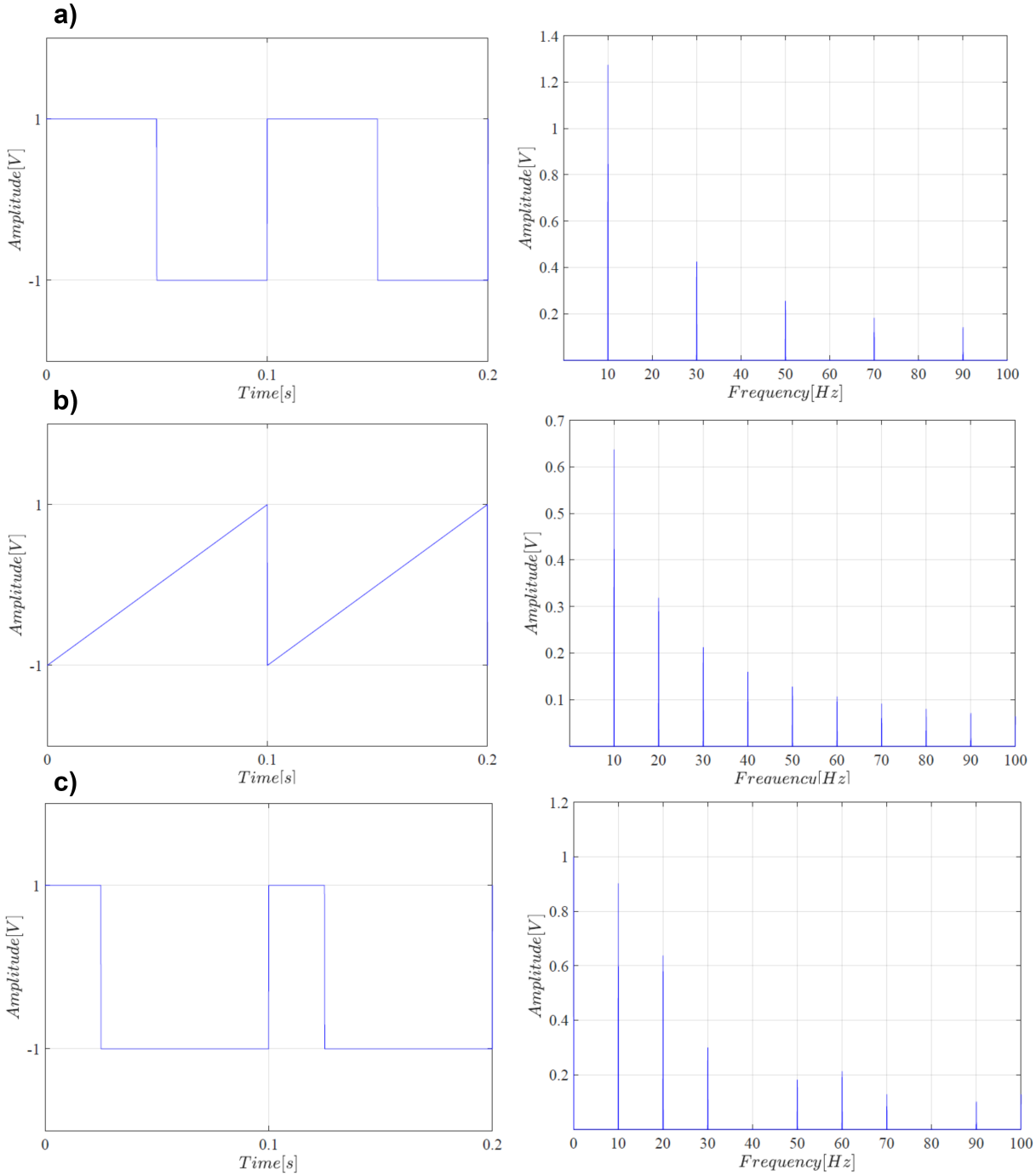

Figure 2.14: Different type of stimulus.

2.2 Additive Manufacturing

The American Society for Testing and Materials organization, or for short ASTM, has defined Additive Manufacturing (AM) as " a process of joining materials to make objects from 3D model data, usually layer upon layer, as opposed to subtractive manufacturing methodologies." [29]. AM is used with various types of materials as metals, polymers, ceramics and many more. AM has been around for many years, but only in the last decade, it has emerged as a fundamental manufacturing technology. Nowadays, AM has grown from being used just for prototypes production to be used towards design final products. AM has some advantages compared to traditional manufacturing methods like faster setup times, being less costly for lower production volumes and enabling building complicated geometries. However, AM didn't come to replace the traditional industry because the AM process still has some disadvantages as, size restrictions, machine investment is typically very high, requires dedicated and potentially expensive materials, low throughput, and the surface quality isn't always the best for a commercialized product, thus requiring post-processing.

2.3 Metal Additive Manufacturing

There are a lot of innovative technologies used in the MAM industry, where the most used technologies are Binder Jetting (BJ), Sheet Lamination (SL), Direct Energy Deposition (DED) and Powder Bed Fusion (PBF). BJ works by depositing a binder liquid, using an inkjet printhead, in the metallic powder to hold the metal powder together. Then layer by layer, the metal powder is added together with the binder liquid to achieve the assembled 3D piece. When the binder dries, the 3D part is still very fragile, and so the produced part is usually cured during six to twelve hours to give mechanical strength. After that, the part is heat-treated at 1100 Celsius for twenty-four up to thirty-six hours to sinter the loose powder and volatilize the binder [30]. The BJ process is shown in Fig. 2.15.

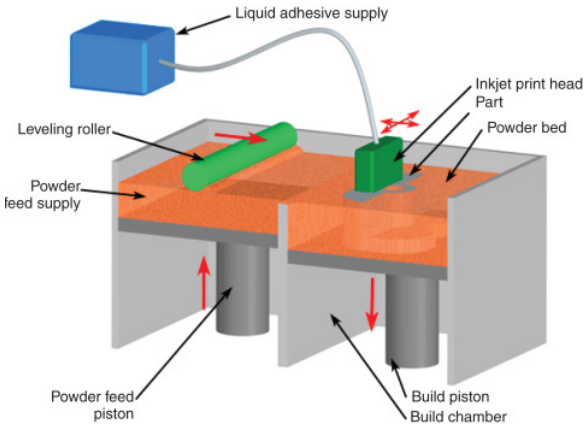

Figure 2.15: Binder Jetting technology. Taken from [13].

SL stacks metal sheets to form a 3D object. After stacking, the metal sheets are either adhesively joined or metallurgically bonded using brazing, diffusion bonding, laser welding, resistance welding or ultrasonic consolidation [31]. Then a laser beam or a drill is used to remove the material to create the desired geometry. A schematic of a SL machine is represented in Fig 2.16 a). The DED technology works by focusing energy to melt powder or wire. Usually, to melt these materials is used a laser, arc or electron-beam source, as shown on Fig. 2.16 b). Then by stacking these melted materials layer by layer, it gives the final 3D object.

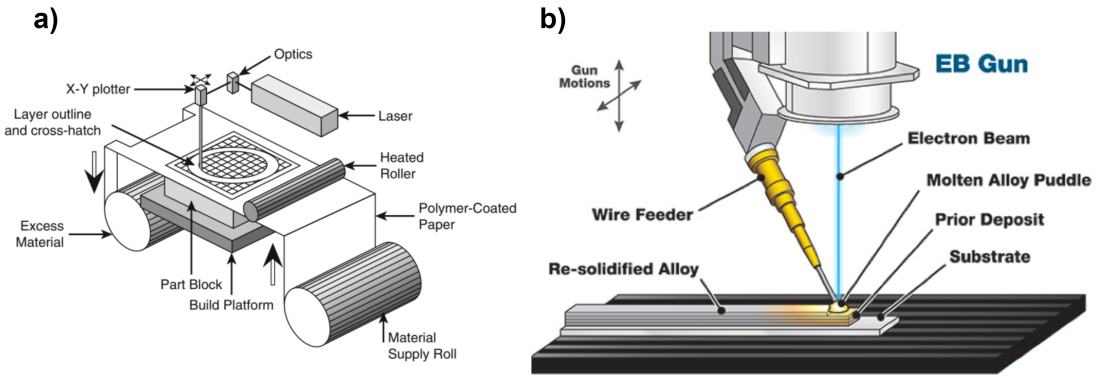

Figure 2.16: SL and DED fabrication processes. Taken from, respectively, [14] and [15].

In this work, the focus will be in the PBF technology, represented in Fig. 2.17. This manufacturing process is used to produce metal additive parts, where the laser energy is used to melt, and consolidate stacked layers from a base metal powder. After a layer is done, the platform is lowered, and a new layer of powder is rolled into the working area. Then the process repeats until the 3D part is created.

The two main methods of focused energy in PBF are the Laser (LPBF), which uses photons to melt the powder, and the Electron Beam (EB-PBF) that uses an electron beam to melt the desired powder into the pretended shape. The laser beam fuses the bed powder at the surface, while the electron beam has more penetration depth into the material. Another difference between these focused energy beams is that the electron beam operates at higher temperatures, usually, than the laser beam, which enables the production with higher melting point materials.

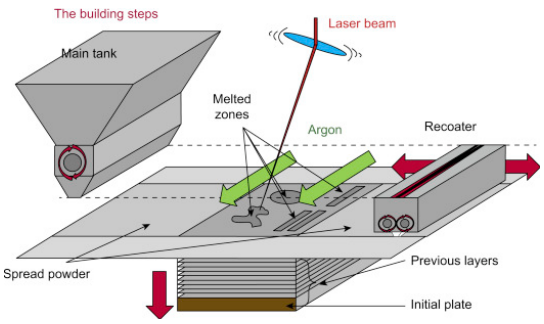

Figure 2.17: Powder Bed Fusion technology. Taken from [16].

2.3.1 Quality Control of PBF

PBF is used to produce parts for the aerospace and biomedical industries, so it is crucial to assure that high-quality standard pieces are fabricated, mainly, on these fields. During a PBF process, surface, geometric, and fusion defects, impurities, porosity, or delamination can occur [32]. To reduce the frequency of occurrence of these conditions, tightly monitored QC systems are used to adjust the PBF process parameters and materials [33]. Optical methods have become popular for PBF QC, where each layer is imaged with co-axial sensing (on LPBF), or through infrared/thermal cameras [34, 35]. Among the non-optical QC methods, the acoustic emission and laser ultrasound methods were tried [36, 37].

In this project, a new approach will be taken, in the quality control of the PBF produced parts by developing an ECT array probe. ECT probes are already used a lot in the NDT industry, and are used, for example, to inspect metal surfaces. Therefore, further developing this technology to a new application can benefit the MAM industry. This ECT array probe's objective will be to ensure the quality of produced parts to detect inconsistencies during the manufacturing process.

2.3.2 ECT Advantages and Limitations on MAM

ECT consists of inducing an electrical current in the material and sensing the resulting magnetic field [38]. It has been used on crack detection [39] and, with probe arrays, for imaging [40]. In PBF, ECT array probes are attached to the machinery recoater, and spatial resolution is determined by the array pitch and the distance between measurements. Coil based arrays with 0.826 mm pitch have been reported [40], and Magneto Resistive (MR) sensor arrays with 500 µm [41] and 125 µm [42] pitch, resulting in effective spatial resolutions around 500 µm. Also, ECT is very versatile, because ECT not only allows crack detection [43], but can also be used for other types of measurements, such as material hardness [44], and material thickness [45] in a large variety of materials.

Another advantage of the ECT in the MAM industry is its reliability for a wide range of temperatures. Also, ECT can perform high-speed readouts from the sensors [46]. Finally, ECT is a field in which new types of probes and techniques are being developed every year due to the demand for higher quality standards in various industries. The most significant disadvantage of the ECT is its susceptibility to magnetic permeability changes, which is why ferromagnetic materials testing can be difficult.

3

Preliminary Design and Coil Testing

Contents

This work's first objective is to study different types of sensitive elements that will be used on the final array probe. In order to accomplish this first objective, hardware and firmware were developed to test the best suitable sensitive elements.

3.1 Hardware

In order to stimulate and interpret the probe signals, it was used the ECF10 module, which was previously developed in the scope of an independent project. This module can be used for various applications such as eddy currents testing, vibro-acoustics or impedance characterisation. The internal architecture of the ECF10 is shown in Fig. 3.1. An MSP430FR2355 from Texas instruments is used for analogue to digital conversion, offset removal, and vector amplification. The MSP430FR2355 is also used to communicate with a PC to analyse the probe's data. There is also a Direct Digital Synthesizer (DDS) AD9838 from Analog Devices, which is used to generate a sinusoidal signal and its inverse. The output channels use a high output current operational amplifier, TH3062 from Texas Instruments.

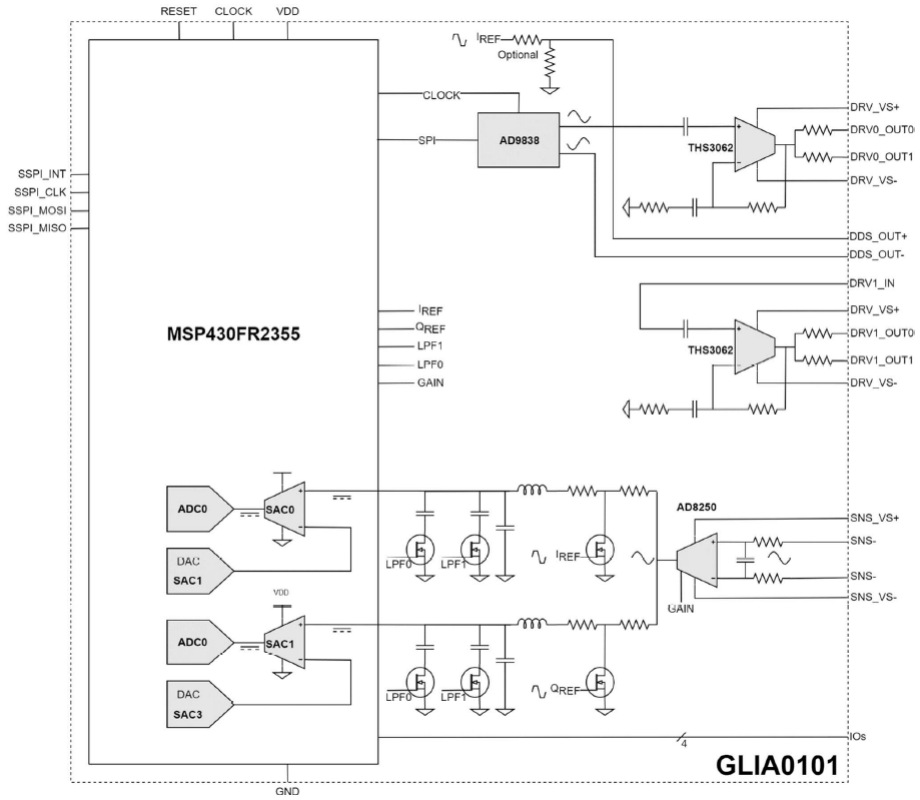

Figure 3.1: ECF10 schematic.

An instrumentation amplifier, AD8250 from Analog Devices amplifies the input signals. The amplifier gain selects from x1, x2, x5, x10, and the input impedance is set to $200\ k\Omega$.

A switched mixer is responsible for the down-conversion of the in-phase and quadrature components of the input signal.To obtain these components, two transistors were used where each one of them had connected a square signal out of phase 90º degrees. In the end, the demodulated signal is filtered by configurable low-pass filter with a cut-off frequency that can be set between 10 Hz, $100\ Hz$ and $1\ kHz$ in order to remove the higher frequencies components. This type of demodulation allows the input signal to be mapped on a real-imaginary axis. This information could be helpful, for example, to estimate the probe lift-off, the material's electric conductivity and defects detection. On Fig. 3.2 is shown the block's schematic for the IQ demodulator.

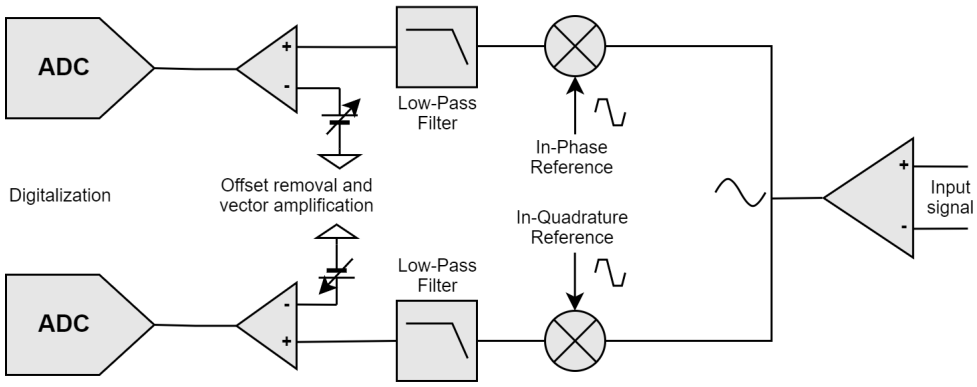

Figure 3.2: Block's schematic for the IQ demodulator.

The preliminary tests of different sensitive elements were accomplished by using the described ECF10 module. But also, two PCB boards were developed to build the test probe. The first board developed was a support board for the ECF10 module. In Fig. 3.3 is shown the support board for the ECF10 module. As can be seen in Fig. 3.3, it was developed a simple support board that has a supply voltage of $\pm 12\ V$. It is composed by three voltage regulators, one programming and communication header, one header to plug the probe, two communication headers and, some bypass and decoupling capacitors.

The second board developed was the sensor board. The topology used in the sensor board was the absolute probe topology. This topology was chosen because it is intended to use the probe to measure conductivity and detect defects. The reference coil's signal is subtracted with the measurement coil's signal before amplifying the signal. Thus the variations at the output of the amplifier caused by the conductivity will be more significant than without a reference coil. In total, there were twenty boards produced so that each board could be used independently with different sensors. On Fig. 3.4 is shown the developed PCB.

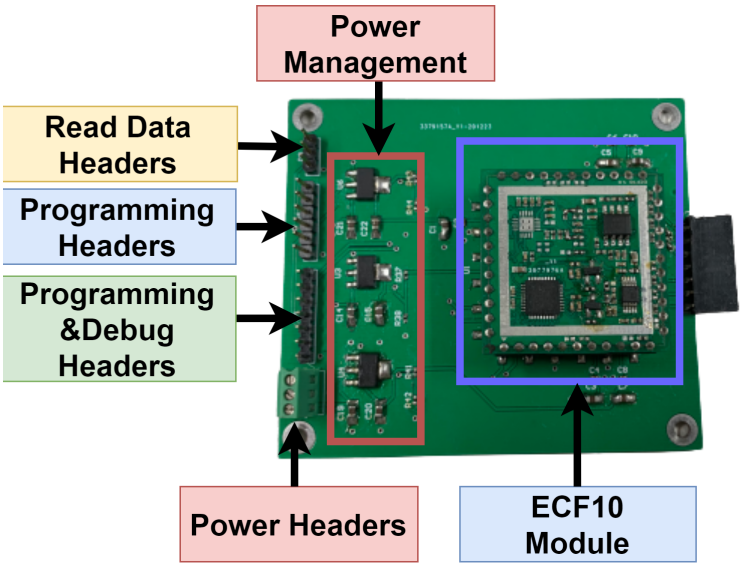

Figure 3.3: Developed support board for the ECF10.

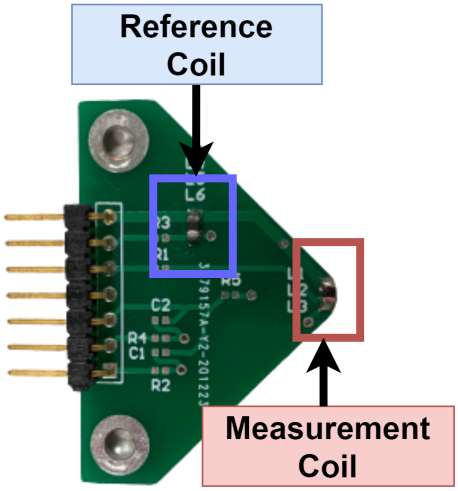

Figure 3.4: Developed absolute probe to test different coils.

In order to test the developed probes, and analyse the materials to decide the best sensing elements, a Computer Numerical Control (CNC) table was used to attach and move the produced probes over different testing samples. This table has two stepper motors that can move in the x-axis and y-axis independently, as it showed in Fig. 3.5. The CNC table can move on the X-Y axis automatically with a max travel distance of 20cm and each axis has a max resolution of 0,05mm. The Z-axis can only be adjusted manually.

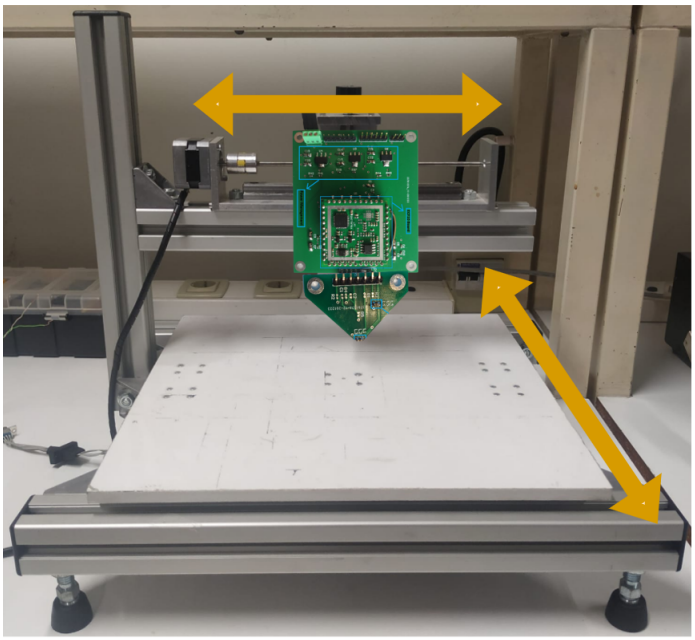

Figure 3.5: CNC table with the support board and absolute probe copulated.

3.1.1 Firmware And GUI

For the initial tests, the firmware used on the ECF10 was previously developed in an independent project. However, changes were made to this program not to use the DDS and instead to use a square signal generated by the MSP430FR2355 to stimulate the absolute probe.

The initial developed Graphical User Interface (GUI) is shown in Fig. 3.6 a), and it is used to control, program and analyse the signals from the probe. In this interface, it can be set the output frequency to stimulate the probe, the input gain for the instrumental amplifier, the bandwidth for the low-pass filter at the output of the demodulator, and the digital gain for the Programmable Gain Amplifier (PGA) inside the MSP430FR2355. From the graphs, the user can visualise the variations for the real and imaginary amplitudes. Finally, in Fig. 3.6 b) is shown the control panel to control the CNC machine. Here the user can control the CNC machine in real-time using the arrows or pre-programming the CNC machine, with the X and Y distances for the probe to travel. If the user pre-programs the X and Y distances and

presses the Start-Auto button, a 2D intensity chart from the analysed material will be obtained.

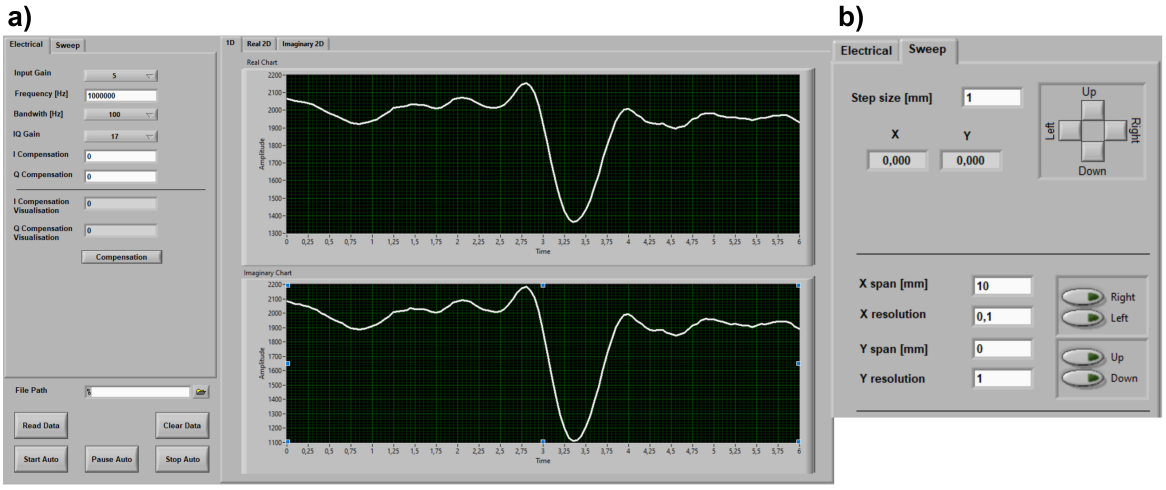

Figure 3.6: GUI for the ECF10 and CNC machine.

3.2 Results

Initial tests were performed to choose the best coils to be used on the final array probe. The list of tested coils is shown in Table 3.1.

Table 3.1: Initially tested coils.

Tested coils					
Nr	Coils Reference	Inductance [μH]	Shielded?	Coil Type	Size
1	LB2012T101K	100	No	Wirewound	0805
2	L0805C101MPWST	100	Yes	Multilayer (Ferrite Core)	0805
3	LB2012T680K	68	Yes	Multilayer (Ferrite Core)	0805
4	LBR2012T470K	47	No	Wirewound	0805
5	L0603B4R470MDWFT	47	Yes	Multilayer (Ferrite Core)	0603
6	LBMF1608T220K	22	No	Wirewound	0603
7	MLF1608C180KTD25	18	Yes	Multilayer (Ferrite Core)	0603
8	LQM18FN100M00D	10	Yes	Multilayer (Ferrite Core)	0603
9	MLF1608A3R3JTD25	3.3	Yes	Multilayer (Ferrite Core)	0603

All coils were tested by making a single scan on a simple defect. Also, preliminary tests were made to understand the system's best operation frequencies, which were determined to be 1 MHz and 1.5 MHz,

which is the biggest frequency that the MSP430 can output. The initial study concluded that the higher inductance coils were more sensitive in detecting the analyzed defect, and the coils with less than 10 μH had more difficulty detecting the same defect.

For the more in-depth analysis, it was decided to use the two coils with more inductance, the 100 μH coils, and it was also decided to use the 47 μH inductance coils because even though they were not the most inductive coils in the list, the shielded coil had a more square format, and so in the more in-depth tests, it was also analyzed if the format of the coils also affects the reconstruction of the defects.

For the more in-depth analysis, an aluminium sample was used to characterize the coils' response. The two defects analyzed on the aluminium sample were a circular defect, and an infinite failure. Fig.3.7 shows the aluminium sample with the defects.

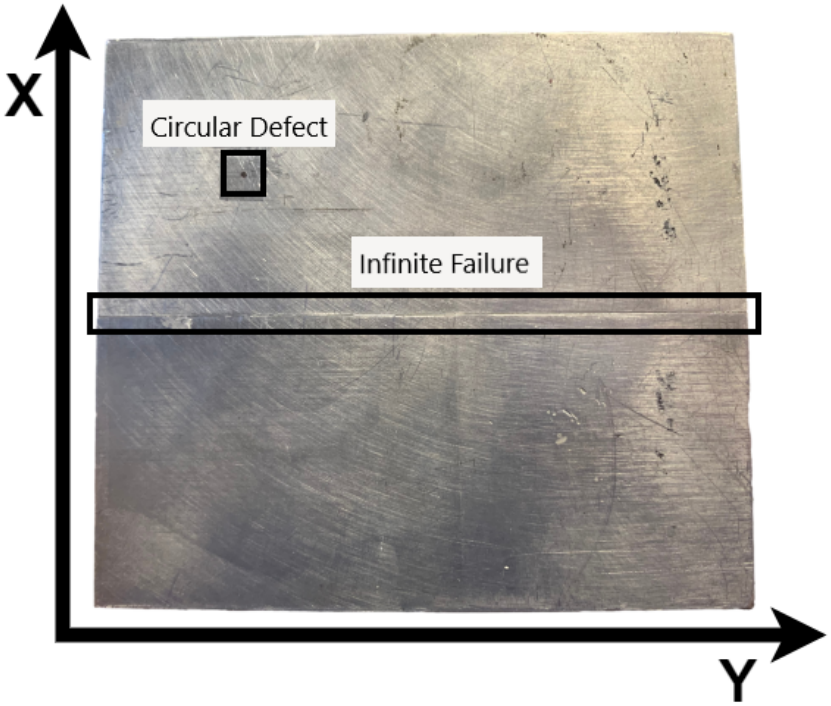

Figure 3.7: Aluminum sample.

The first analysis to test the four coils was made in the infinite failure. Fig. 3.8 presents the defect analysis for a specific Y-coordinate because the defect is constant across the Y-axis. However, on the Appendix A (Chapter 6) shows the 2D imaging of the defect for the four coils and the respective real-imaginary components for 1 MHz (blue line) and 1.5 MHz (red line) frequencies.

The second test performed was in the circular hole, also with a stimulation signal of 1 MHz and 1.5 MHz. In Fig. 3.9, is shown the results for the four coils, but only for the 1 MHz frequency because better results were achieved for this frequency. In appendix A (Chapter 6) is shown the same tests but for the 1,5 MHz frequency, and respective 2D imaging.

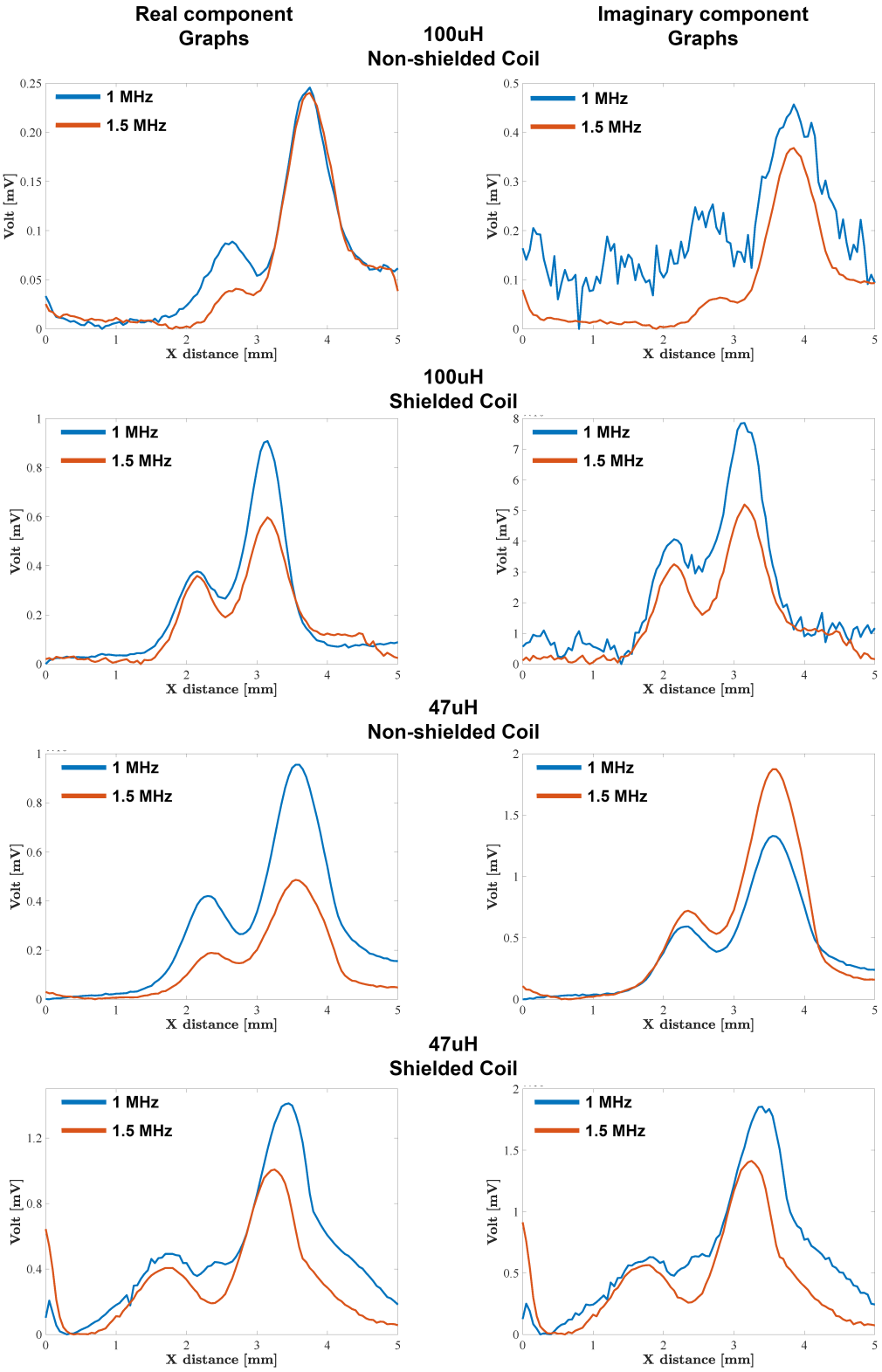

Figure 3.8: Infinite failure analysis.

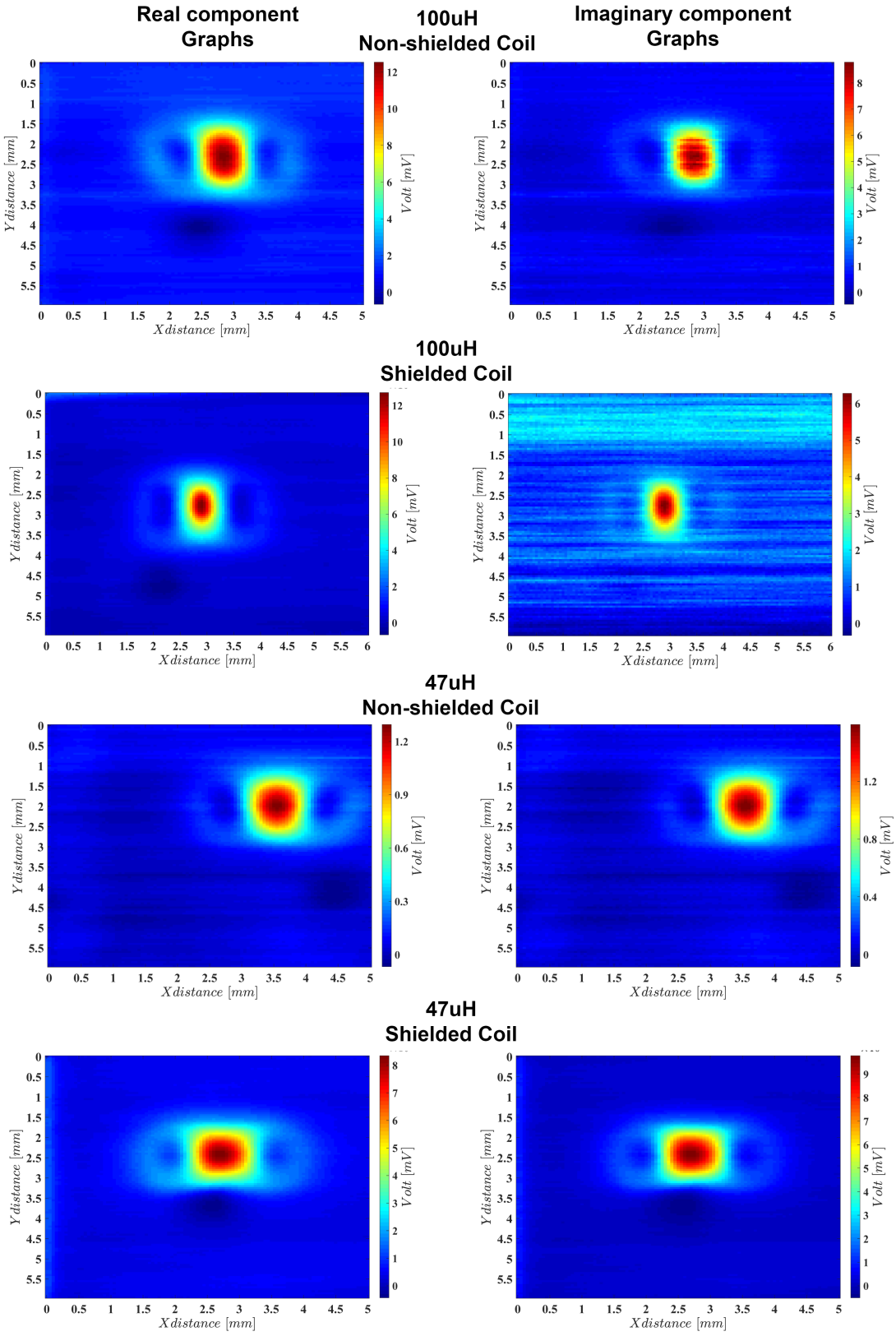

Figure 3.9: Circular hole analysis.

From Fig. 3.8, and analyzing the figures, it is observable that almost for all coils, the best frequency is 1 MHz because when the coils pass through the defect, there is a more considerable voltage difference. It is also noted that for the 100 μH shielded coil, the voltage difference is almost 8 mV. From the 2D imaging analysis in Appendix A, it is observable that the defect is more constant for the shielding coils as expected.

Analyzing the 2D imaging for the circular defect with different coils shows that the coils were more sensitive for the 1 MHz frequency. However, this time better results were obtained by the 100 μH coil because there is a more considerable voltage difference with this coil. Nevertheless, the 100 μH shielded coil reconstructed a more similar defect as the one on the aluminium sample. The 47 μH coils had the worst results for the infinite failure and the hole defect, but interestingly, some holes are more squared than others because of the shape of the coils, in this case, the 47 μH shielded coil had a square shape, so that shape was mirrored into the final result.

In the end, because better results were obtained with the 100 μH shielded coil, this coil will be used as the sensing element for the final array probe.

4

Final Design and Evaluation

Contents

In this chapter, a probe was initially made, which represents a channel of the final array probe. This probe was developed to reduce as much hardware as possible and thus reducing the costs per channel without compromising the final array probe performance. The second part of this chapter presents the array probe and the respective GUI to interpret the signals from the probe. Finally, the results obtained with the array probe are presented.

4.1 One Channel Probe Design

4.1.1 Hardware

The developed one channel probe has a supply voltage of 3.3 V for the MSP430FR2355, 5 V to supply the operational amplifier and a GND reference. The MSP430FR2355 is used to stimulate the compensation and stimulation coils. The coils are in series with a 100 Ω resistance to limit the current from the MSP430FR2355 to the coils. The signal amplification from the coils is achieved using a differential amplifier set, initially, with a gain of 10. Two transistors are also responsible for converting the in-phase and quadrature components, passing then through a 1 kHz low-pass filter. In the end, inside the microcontroller, the remaining signal is subtracted by an offset voltage, which is subsequently amplified by a PGA and then digitalized by an Analog-to-Digital Converter (ADC). In Fig.4.1 is shown a picture of the one channel probe PCB.

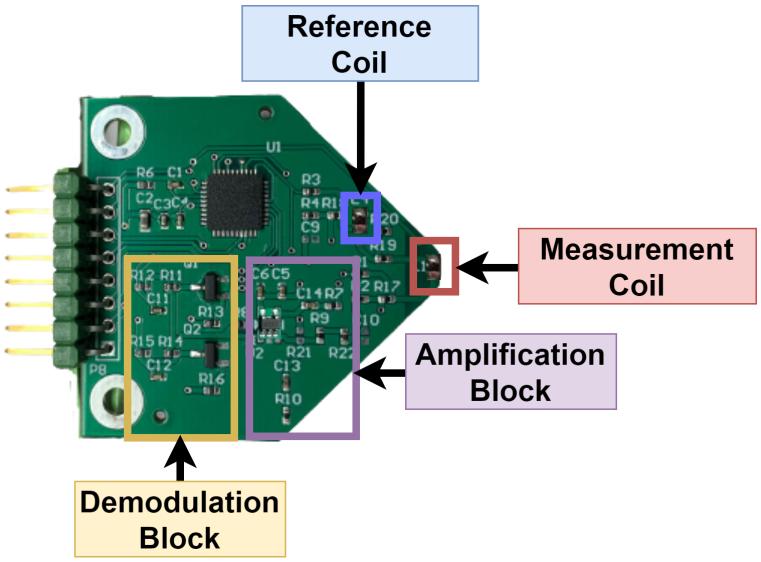

Figure 4.1: One channel probe PCB.

4.1.1.A Probe channels

The probe channel was developed to test different configurations in the signal conditioning and stimulation of the coils. However, after some tests, some changes had to be made. The first thing noticed was that the MSP430 did not have enough Input/Output (I/O) ports to use two timers to generate a Pulse Width Modulation (PWM) to drive the coils in a bipolar fashion as initially thought, and so unipolar driving was used by connecting one of the coils pad to ground. The second change was changing the 100 Ω input resistance for 270 Ω because the current coming from the MSP430 was too high, so the resistance had to be higher to conditioning the current coming from the MSP430. Also, the low pass filter was removed because, after some tests, it was noticed that it would not be necessary to filter the signal from the coils. In Fig.4.2 is shown the final schematics for the probe driver and compensation.

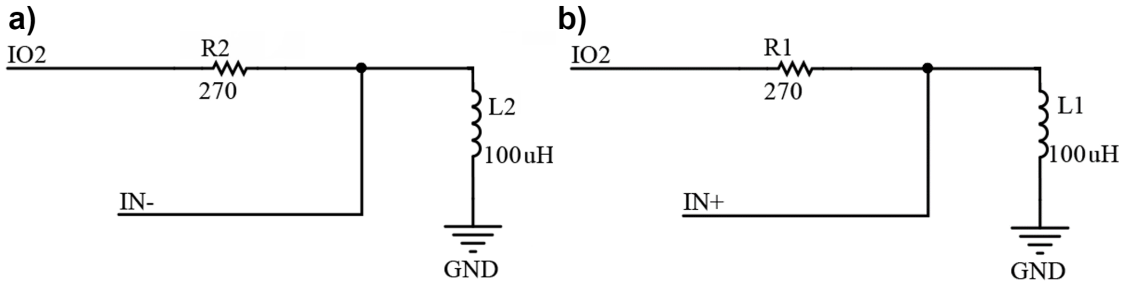

Figure 4.2: Final design for the stimulation and compensation coil.

4.1.1.B Signal amplification and Demodulation

Fig.4.3 shows the initial schematics for the amplification and demodulation of the probe response.

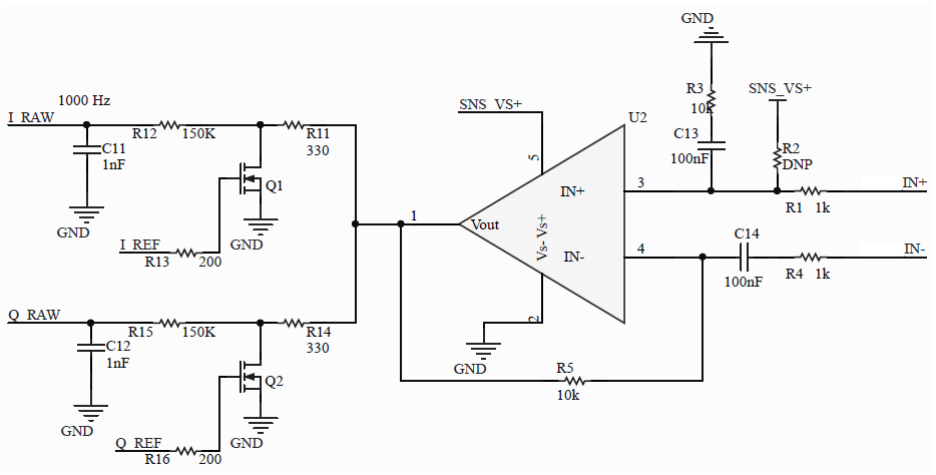

Figure 4.3: Schematic for amplification and demodulation of the probe response.

Initially, for the amplification part, the Operational Amplifier (Op-amp) had to be chosen. The initial tests, made in chapter 3, were conducted by stimulating the coils with a 1 Mhz or 1.5 Mhz signal and using a programmable gain instrumentation amplifier to amplify the signal's difference between the compensation, and the stimulation coil, with a gain set to 10 or 100. By knowing this information, the operational amplifier for the new PCB should have a gain-Bandwidth Product (GBW) between 15 Mhz (10 x 1.5 Mhz) and 150 Mhz (100 x 1.5 Mhz).

Another requirement for the Op-amp was to have a rail to rail and single-supply operation, so it could be possible to power the amplifier between ground and 5 V. It was also crucial that the chosen Op-amp had a high Slew-Rate (SR), a high Common-mode Rejection Ratio (CMRR) and a low total harmonic distortion. All the compared Op-amps are in Table. 4.1. It was decided to use the GS8051 amplifier even though there are better options in the mentioned list. Some amplifiers had to be discarded due to the current chip shortage, and from all the research, the GS8051 was the cheapest amplifier that met all the requirements.

Table 4.1: Op-amp list.

Op-amp list						
Op-amp reference	GBW [MHz]	Vos [mV]	Ib [μA]	CMRR [dB]	SR [V/μs]	Price per unit [€]
MAX4452	200	0.4	0.8	-100	95	0.94
AD8051	110	1.7	1.4	-80	145	2.26
RS8751	250	1.5	1	-85	180	0.22
MS8051	250	2	6	-80	93	0.22
GS8051	250	2	1	-80	77	0.15

The initial gain was set to 10 and being a differential amplifier, the initial gain is set by

$$V_{out} = -V_{IN-}\left(\frac{R_5}{R_4}\right) + V_{IN+}\left(\frac{R_3}{R_3+R_1}\right)\left(\frac{R_4+R_5}{R_4}\right), \tag{4.1}$$

and by having $R3 = R5$ and $R1 = R4$, the amplifier gain equation can be simplified to

$$V_{out} = \frac{R_5}{R_4}\left(V_{IN+} - V_{IN-}\right). \tag{4.2}$$

However, after some tests, the results achieved by the amplifier were not great because the output was constantly saturating. This problem was being caused by the impedance differences between the two inputs of the differential amplifier. This impedance matching is important because when the probe is "resting", without having contact with any material, both signals should cancel each other. By trying

to match the input impedances as much as possible is avoided load unbalancing of the measurement and reference coils. In this case, because the input impedance difference between both inputs was very high, different voltage drop showed on each input node of the amplifier, which when amplified lead to the amplifier saturation.

So, in order to solve this problem, the positive channel was connected to a reference of 2.5 V, the voltage divider was set with 24 kΩ resistances, and a capacitor was placed in series for filtering any Direct Current (DC) component. The final schematic for the amplification block is shown in Fig.4.4. The final gain of the differential amplifier is set to 50.

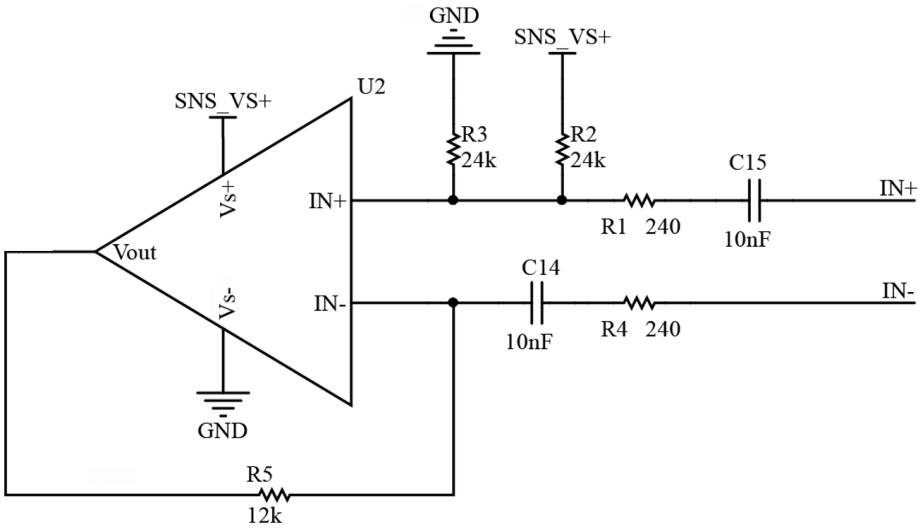

Figure 4.4: Final schematic for amplification block.

For the demodulation block, the change made was the removal of one channel from the demodulator. This removal was made because the objective is to have the minimum amount of hardware as possible in order to reduce space and costs in the final array probe.

4.1.2 Firmware

The ECF10 base firmware was used in this new probe as an initial sketch, but only the communication, interface modules and the compensation command were used in the end. The rest of the firmware changes will be mentioned in this chapter.

4.1.2.A Probe excitation and demodulation

A square signal is generated by the MSP430 using the internal timers of the microcontroller. One timer is used to stimulate the compensation and stimulation coil, and another timer is connected to the transistors' gates.

The square signal is generated by programming the registers CCR0, CCR1 and CCR2. The first register (CCR0) defines the value until where the timer counts, completing an entire cycle. The other two registers (CCR1, corresponding to IO1 and CCR2, corresponding to IO2) hold the values when the square signals outputs change from high to low. The following formula obtains the frequency code that is saved in the register CCR0

$$Freq_{code} = \frac{Freq_{clock}}{Freq_{out}} - 1. \tag{4.3}$$

For our example, the square signal is set to 1 MHz, corresponding to the variable $Freq_{out}$, and the clock source is set to 24 MHz, corresponding to the variable $Freq_{clock}$. In this case, the value saved to the register CCR0 would be 23, and in the other two registers to have two square signals in phase, the value saved would be half of the $Freq_{code}$, which in this case would be 12. To have two square signals out of phase by 90º degrees, CCR0 would equal 23, CCR1 equal 12, and CCR2 equal 0.

4.1.2.B Phase rotation and Auto phase shifting.

Initially, two transistors were used for the demodulation, which made it possible to map the material under test on a real-imaginary axis. In Fig. 4.5 is represented the acquired signal by the microcontroller, on real-imaginary axis, at the circuit outputs shown in Fig. 4.3.

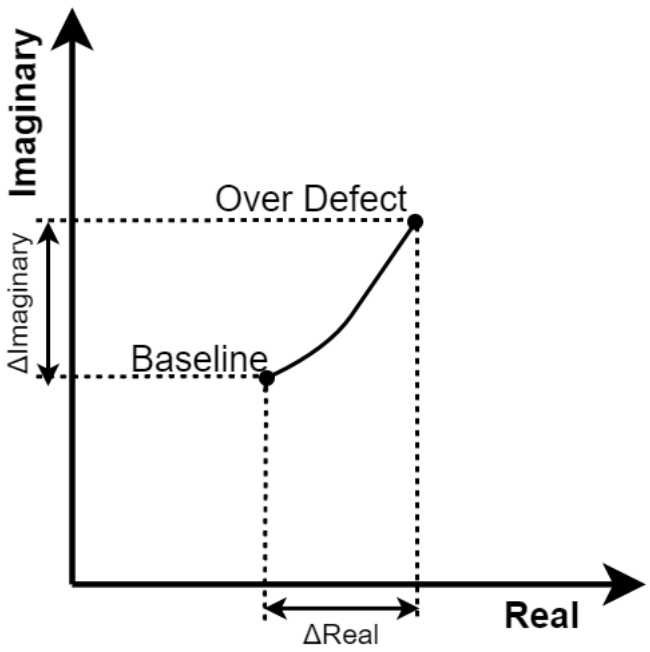

Figure 4.5: Defect detection represented on a real and imaginary axis.

However, there will only be one transistor in the final prototype for the signal demodulation, and so

by demodulating the signal with a single phase reference, some information will be lost. In order to lose the minimum amount of information possible, the phase rotation between the demodulation signal and the stimulation will have to be adjusted to maximize the signal amplitude at the demodulated phase reference, as can be observed in Fig. 4.6 a), where the axis is rotated. In Fig. 4.6 b) is represented the amplitude differences of the real and imaginary part through space. In black is represented the real-imaginary components without axis rotation adjustment and in red with axis rotation. For this example, when the phase rotation occurs, the real part component increases, but the imaginary part gets close to zero.

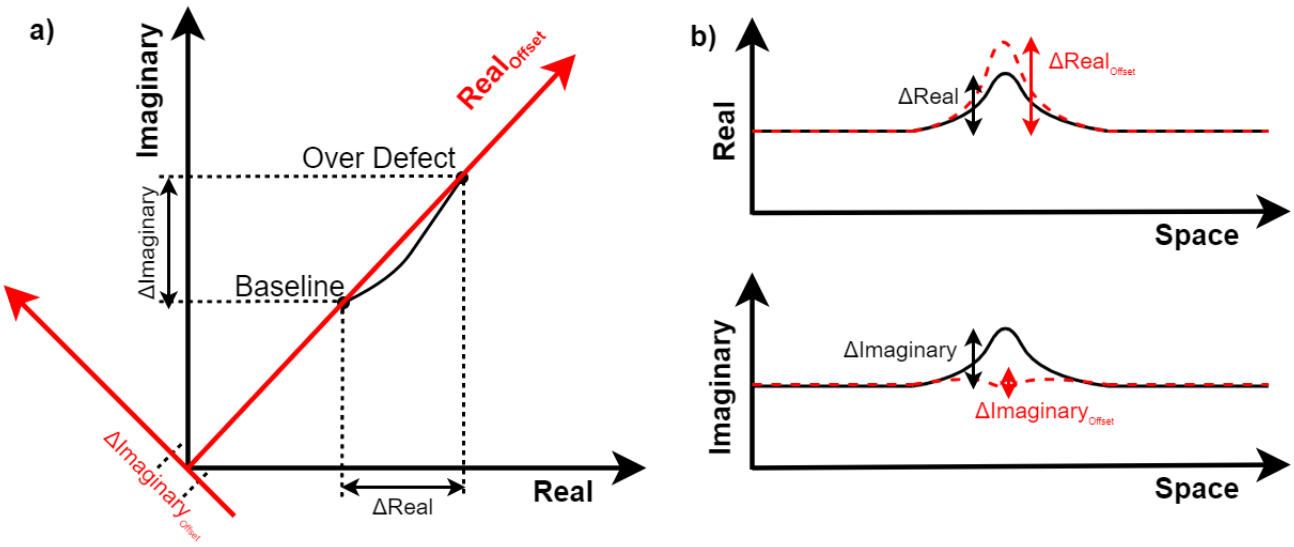

Figure 4.6: Defect detection represent on a real axis.

That is why a firmware algorithm was developed to automatically adjust the phase difference between the demodulation and stimulation signal. The algorithm works by initially shifting only the phase of the demodulation signal and acquiring all the data as the phase signal is changing on top of an area with no defect. After making all the phase combinations possible, which for a 1 MHz stimulation/demodulation signal has 24 possible combinations. The probe is moved to a place where exists a defect, and the same process is repeated. In the end, the initial acquisitions are compared against the final ones, and the best value for the phase rotation is obtained where was a more considerable difference between acquisitions.

4.1.2.C SAC inverting mode

The MSP430 integrates four Smart Analog Combo (SAC)s, and each SAC has inside a low-power Op-amp, a PGA with a gain up to 33, and a 12-bit Digital to Analog Converter (DAC). So, before the demodulated signal gets acquired by the ADC, the signal passes through the SAC.

Initially, the MSP430 was set to use two SACs per channel, as shown in Fig. 4.7, because it was thought that the inverting mode topology had a low input impedance, and so the DAC signal would pass through a buffer before the signal difference between the DAC and the demodulated signal was amplified to increase the input impedance. It is important to note that the low-pass filter has a high impedance, so the input impedance of the digital amplifier has to be high too. Otherwise, the signal would be attenuated. However, after some tests, it was observed that the SAC only in inverting mode had good results too, which meant that the SAC in inverting mode had a high impedance.

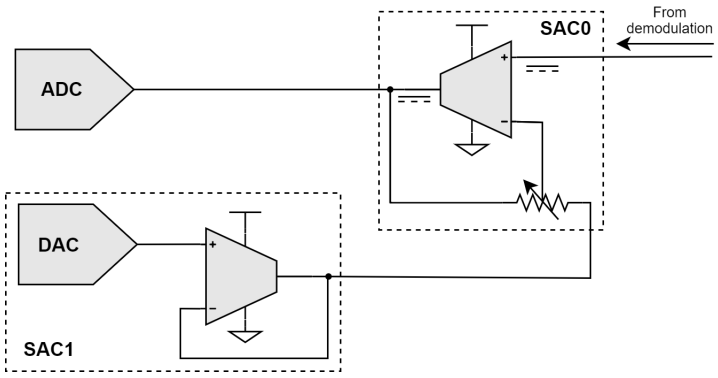

Figure 4.7: SAC combo in buffer and inverting mode.

So, in order to optimize the number of channels per MSP430 in the final array probe, only one SAC was used per input channel so that in the final array probe could be possible to connect four channels per MSP430. In this way, for this project, the SACs were set to be used in inverting mode, as shown in Fig. 4.8.

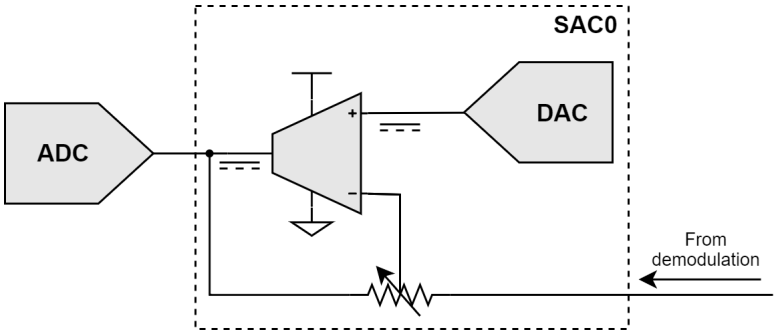

Figure 4.8: SAC in inverting mode.

By choosing this mode, the input signal is initially amplified by the PGA where the user digitally controls the gain up to 33x. Then, the Op-amp amplifies the signal difference between the DAC and the amplified input signal's. By making the offset removal, the signal's difference can be more amplified, which allows to explore better the dynamic range of the ADC.

4.1.2.D Configuring the ADC

The MSP430 only has one ADC, and the ADC is responsible to digitally convert one channel. The MSP430's ADC can be set to 10 or 12-bit analogue-to-digital conversions and have a maximum sampling rate of 200 kSamples/s. The ADC is set to work on single-channel conversion converting each channel one by one, in a total of 4 channels, with 12-bit conversions. The interrupt to acquire each acquisition were triggered automatically over hardware everytime the timer TB1 reached the maximum count value. If in alternative, any software mechanism involving the CPU intervention was used, it wouldn't be possible to ensure that the sampling instants would remain exactly equally spaced and coherent with the excitation signal.The timer TB1 was set with a frequency of 20 kHz, this means that the ADC has a sampling rate of 20 kSamples/s for only one channel. The ADC also has a reference voltage of 2.5 V.

4.1.2.E Moving Average Filter

A moving average filter was programmed to filter the acquisitions. Each MSP430 has four buffers implemented to write each channels acquisitions to the respective buffer. When the buffers are full, it starts to overwrite the data from the initial to the last position of the buffers. When the user wants to read the acquired data, a command is sent to the microcontroller. After that, all the buffers positions are summed and sent to the computer and, then the LabVIEW program makes the average of the sums, filtering all possible outliers.

In order to have a fast system, when the system is turned one, the ADC starts to make acquisitions and writes the information to the buffer without the user input. This way, when the user sends a command requesting for the acquisitions, all the data contained in the buffers is sent, making the start and stop commands obsolete.

After some changes on the hardware and firmware, in fig.4.9 is shown the block's schematic for the final one channel probe with all the changes made during the chapter 4.1.

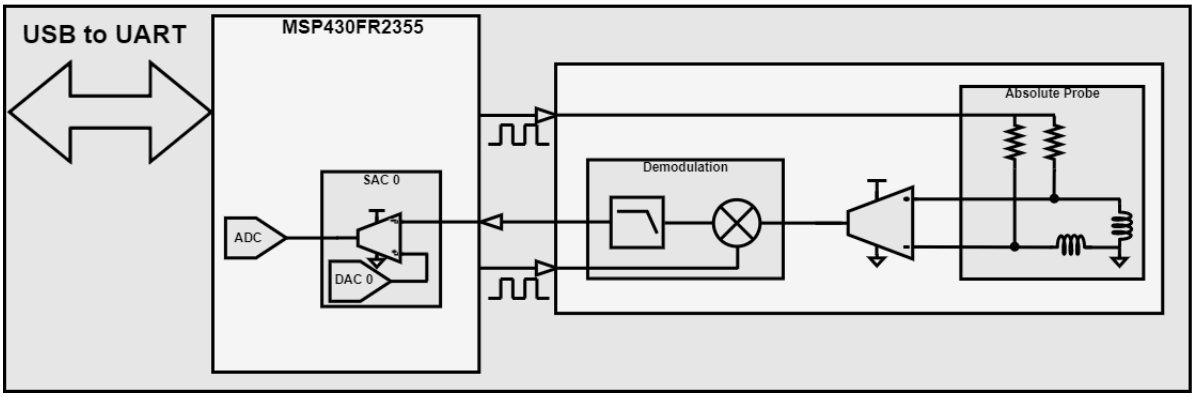

Figure 4.9: Final block's schematic for the final one channel designed probe.

4.2 Array Probe Design

The objective is to develop a probe that is cost-effective and capable of being replicated by integrating multiple coils side by side and able to measure and detect defects on the materials under testing. For this project, only one module with 16 channels was developed. However, the future objective would be to interleave and offset array probes to reduce the space between coils and increase resolution, and increase the analysis area by joining array probes side by side. The final array probe block's schematic and PCB are respectively shown in Fig.4.10 and Fig. 4.11. The probe is divided into five blocks: the power management; the probe channels, which consists of sixteen channels; the processing block, which is composed of four microcontrollers and the FTDI FT4232 mini-module, which is a Universal Serial Bus (USB) to Universal Asynchronous Receiver-Transmitter (UART) converter; the oscillator; and the programming/debugging headers. In Table. 4.2 is showed the array probe specifications.

Table 4.2: Probe Specifications.

Probe size	80x80mm
Coils pitch	5mm
Supply voltage	0-12V
Acquisition rate	20 kSamples/s
Acquisition rate per channel	5 kSamples/s
Demodulation and stimulation frequency	Up to 1.5 MHz
Internal clock and external oscillator	24 MHz

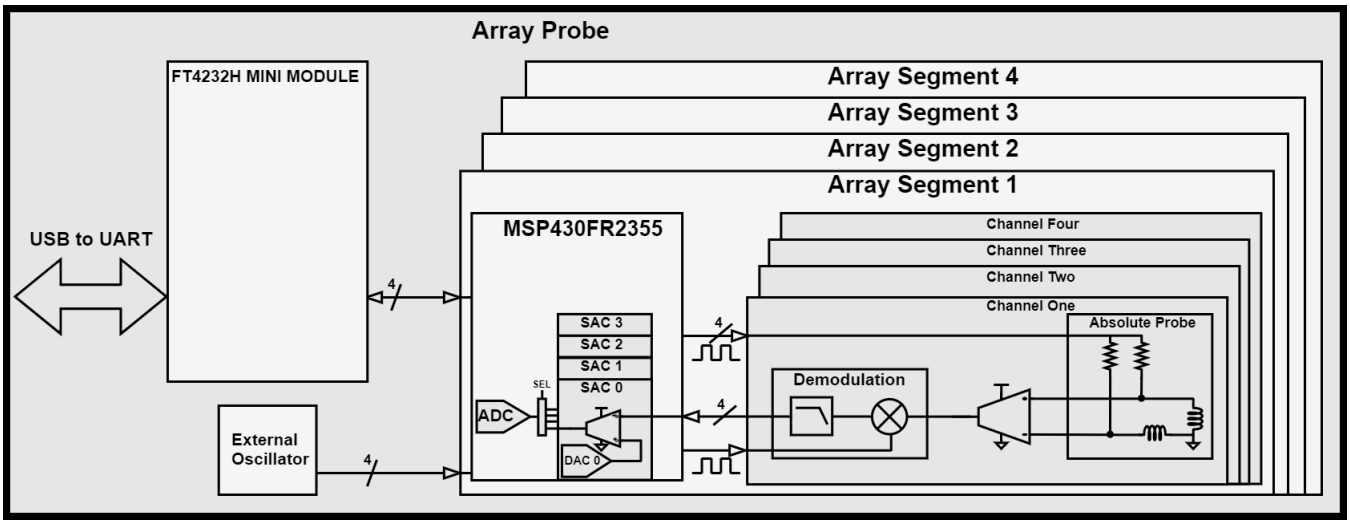

Figure 4.10: Block's schematic for the final array probe.

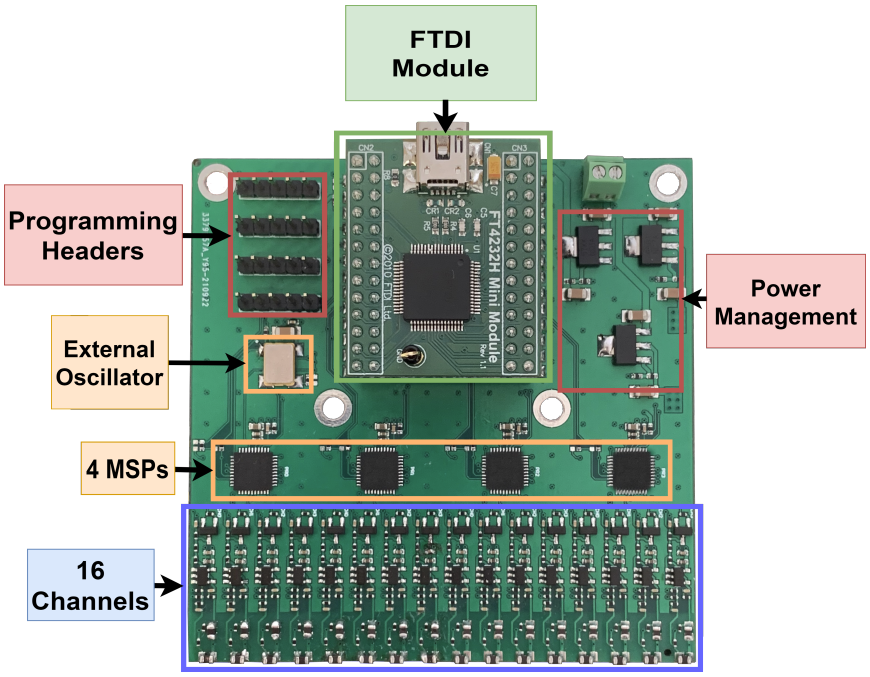

Figure 4.11: Array probe PCB.

4.2.1 Hardware

4.2.1.A Power Management

The array probe has an input supply voltage of 0 V to 12 V, connected to three linear voltage regulators, LM317. One of the voltage regulators converts the input voltage to 3.3 V, and the other two convert to 5 V. These two voltage regulators supply a 5 V because one of the 5 V supplies the digital part of the probe, which is the FTDI mini-module and the other 5 V supplies the analogue part of the circuit, in this case, the Op-amps. These 5 V supply voltages are decoupled in order to create fewer interferences in one another. The 3.3 V supplies the four MSP430FR2355. Each MSP430 has a power consumption of 200 mW and the total power consumption of the system is 3 W.

4.2.1.B Probe channels

As mentioned before, the probe consists of sixteen channels. Each channel is composed of two coils, one compensation and one stimulation/sensing coil, a differential amplifier with a gain set to 50, a transistor to demodulate the Op-amp signal difference, and a low pass filter set with a cut-off frequency of 1 kHz.

For the final array probe, it was decided to use the 100 μH shielded coils due to their better sensibility in detecting and reconstructing the defects analysed in chapter 3.2.

4.2.1.C Processing block

Four microcontrollers and the FTDI mini-module FT4232 constitute the processing block. Each microcontroller is responsible for acquiring the data from four channels, in a total of sixteen channels. Each one of the microcontrollers is responsible for stimulating four channels, control the demodulation signals and obtaining each channel's information. After acquiring the data, the data is sent to the FT4232 mini-module. The FT4232 is responsible for receiving all the data from the four microcontrollers. The communication between the four MSP430FR2355 and the FTDI mini-module is achieved by using the UART communication protocol. After receiving all the information, the FT4232 mini-module sends the information to the computer by USB using the USB protocol communication.

4.2.1.D Oscillator

In all the tests made, it was only used one MSP430FR2355 in each PCB, and because of that, the microcontroller's internal oscillator was used for the stimulation and demodulation. Now, for the final PCB, there are four microcontrollers. So is essential that all the MSP430 have the demodulation and stimulation synchronized between them. Otherwise, if independent demodulation and stimulation sources were used, their frequency differences and drift could result in cross-channel interferences. Those interferences would result in a low-frequency beating, whose frequency would equal the frequency difference between adjacent channels. The external oscillator works at a frequency of 24 MHz.

4.2.2 Software

4.2.2.A Protocol Communication

As mentioned in chapter 4.2.1.C the communication between the FTDI module and the four MSP430 was made by using the UART port. In Table.4.3 is shown the structure of the data package for the communication between the MSP430, the FTDI module, and subsequently the PC.

Table 4.3: UART package structure.

Data Pack structure					
Command code	Value send	Data size	Data	CRC code	End of package code
1 byte	4 bytes	1 byte	Up to 256 bytes	1 byte	1 byte

The first command defines which function will be used by the MSP430, and the second command is the value written onto the microcontroller used by the command function. The data command corresponds to the data sent from the MSP430 to the FTDI module, but the data size has to be defined

with the data size command. The CRC code command is used to verify if the data was correctly sent and received, and the last command is used to tell the microcontroller and the PC that the end of the package has been reached.

In Table 4.4 is shown the five commands used to communicate with the MSP430.

Table 4.4: MSP430 commands.

MSP430 commands	
Command name	Command code
Read command	0x20
Frequency command	0x32
Digital gain command	0x34
Calibration command	0x38
Compensation command	0x3A

Read command is used to retrieve the data from the MSP430. ***Frequency command*** is used to adjust the stimulation and demodulation frequency, and frequency up to 1.5 MHz can be set. ***Digital gain command*** sets the gain for the internals PGA of the MSP430, where a maximum gain of 33x can be set. ***Calibration command*** is used to adjust the phases between the demodulation and stimulation signals to make the probe more sensitive in detecting defects, as explained in more detail in chapter 4.1.2.B. ***Compensation command*** is used to compensate each probe channel by adjusting the DAC's value of the microcontroller so that the converted digital amplitude in each channel for the initial position is close to 2048. This way, when the channels detect some defect or interferences, the converted digital value will vary between 0 to 4096, being the converted value 2048 a position without defects. Summarizing this command is used to set the initial position of the array probe as the comparison point for the other points of the test material that will be analyzed.

4.2.2.B Labview GUI

A PC application was developed to communicate with the array probe and the CNC machine using LabVIEW 2020. The GUI allows the user to configure the array probe parameters like the stimulation and demodulation frequency and the gain of the PGA inside the MSP430, and there is also the Calibration and Compensation buttons. All the commands were explained in more detail in chapter 4.2.2.A.

The GUI also lets the user check the status of the array probe and the CNC machine in case some error occurs during the programming and use of the probe and CNC. Also, if a file path is given, the acquired data can be exported to a .mat file.

The developed Labview program also lets the user to control the array probe manually or automatically. On the manual mode, the user only has to put the number of acquisitions needed and press the ”Read Data” button.

For the automatic mode, the user has to use the interface in Fig. 4.12 b). The user has to give the X-Y travel distance, the number of steps for each axis, and the X-Y direction, and so an intensity chart from the analysed material will be obtained by pre-programming this information and pressing the ”Start-Auto button”. It is also possible only to move the CNC machine using the arrow keys.

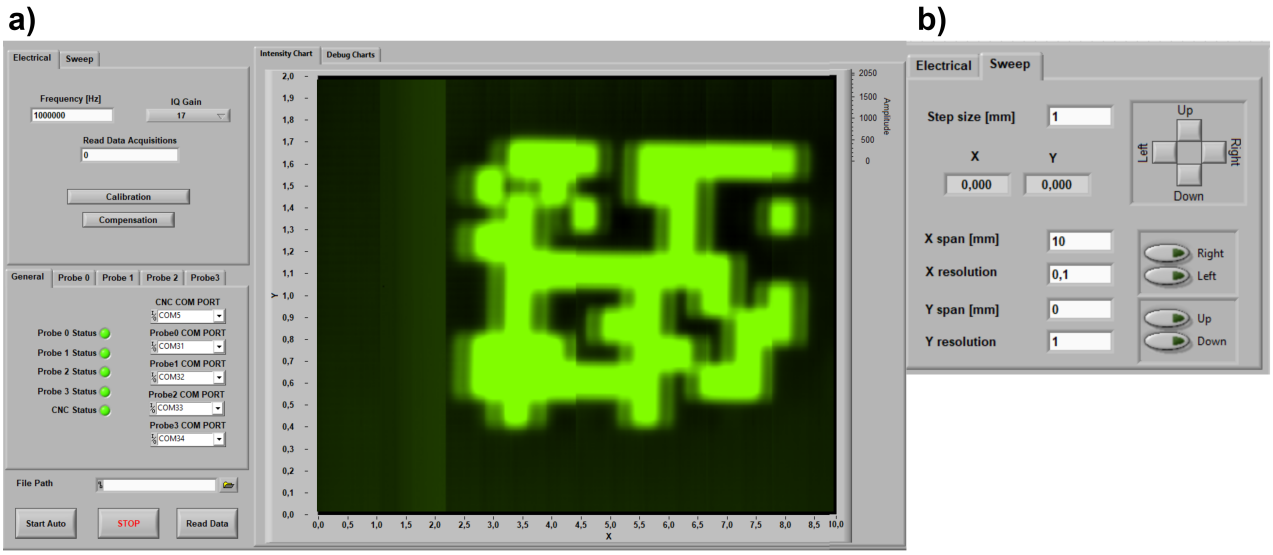

Figure 4.12: GUI for the array probe and CNC machine.

4.2.3 Results

In this section, the developed system is tested by analyzing different types of patterns. The developed array probe will be tested with 100 μH shielded coils. For all the tests conducted a stimulation and demodulation frequency of 1MHz, a digital gain of 17, and an analogue gain of 50 were used.

The analyzed patterns were developed in another project. Each pattern is printed in a 100x100mm PCB. The less dark blue zones of the PCBs are the area where exists metal, and the darker zones are zones where the metal was removed. Each PCB has a 1mm metal layer thickness. These metal layer patterns are not the final target for the probe to analyse, but they allow to show that the system can reconstruct different types of patterns.

The first pattern analyzed was the square pattern. The biggest square pattern has a side of 25x25mm, and the inside square has a side of 15mm. In Fig. 4.13 a) is represented the 2D imaging obtained by the array probe and in Fig. 4.13 b) is shown the pattern analyzed. The reconstructed square has a more rectangle shape because the probe response is not omnidirectional, and so the reconstructed pattern stretches to the X direction. The square pattern has a distance between metals of 5mm, and the reconstructed pattern has a respective distance of 4.8mm and 4mm, as can be observed in Fig. 4.13 a).

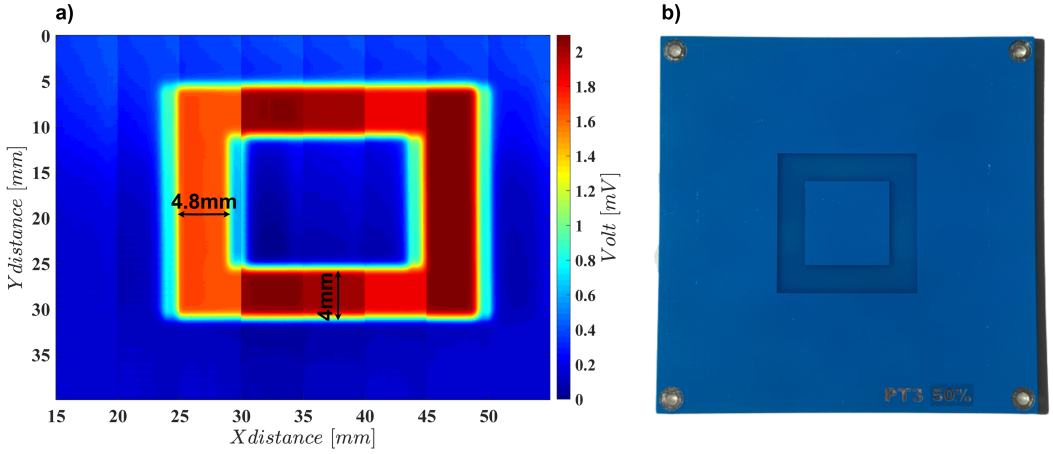

Figure 4.13: a) 2D imaging of a square pattern and b) Analyzed square pattern.

The second pattern analyzed was the circle pattern. The biggest circle pattern has a 25mm diameter, and the inside circle has a diameter of 15mm, which means a distance between metals also of 5mm. Fig. 4.14 a) shows the 2D imaging of the pattern and Fig. 4.14 b) the respective pattern. The reconstructed circle also has a more oval shape also, due to the probe response being not omnidirectional.

From the analysis of the two 2D imaging figures, a pattern starts to be noticed, which is the colour variation between different channels. Some channels are more sensitive than others because of the coils lift-off due to difficulties when hand-soldering the coils, making some coils closer or further away

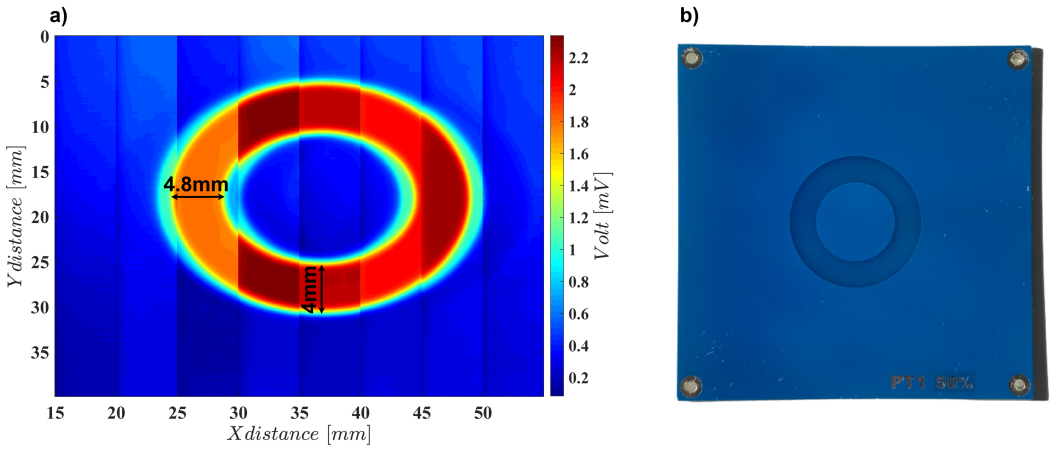

Figure 4.14: a) 2D imaging of a circle pattern and b) Scanned circle pattern.

from the test material. The redder zones are the zones where the coils are closer to the test material. In Fig. 4.15, it can be observed that some channels coils are a bit closer and others farther away from the test material.

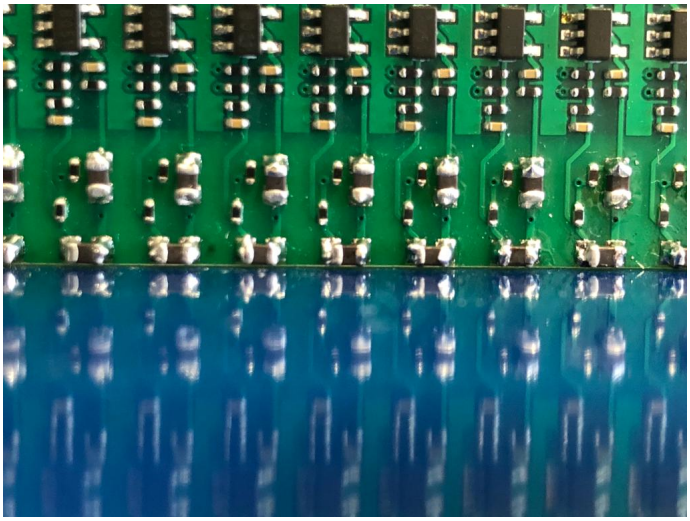

Figure 4.15: Misaligned coils.

A sensitivity offset value can be given to each channel to solve this problem to compensate for the distance between coils to the test material. Eventually, this problem could be solved by using an automated soldering machine. However, even if that could not solve all the channels offset, a simple calibration process could solve it by using a known test material and then fine-tuning each sensitive element manually or automatically for that known material. In Fig. 4.16 is shown the already analyzed patterns but with a compensation value on the post-processing data for each channel.

The third pattern analyzed was a squared QR code with a 50mm side, with square patterns as small

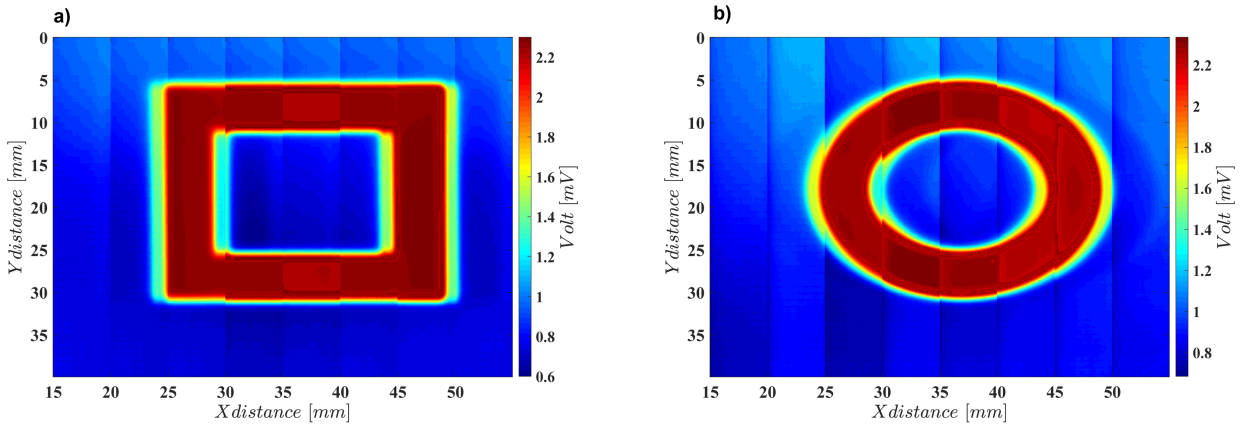

Figure 4.16: Square and circle 2D imaging with channel compensation.

as 5mm. In Fig. 4.17 a) is the obtained 2D imaging and Fig. 4.17 b) the scanned pattern. This pattern was used to test if the array probe could detect patterns close to each other. By analyzing the 2D imaging image, it is possible to observe that the array probe detects well the patterns, but the metal layers between patterns are less noted.

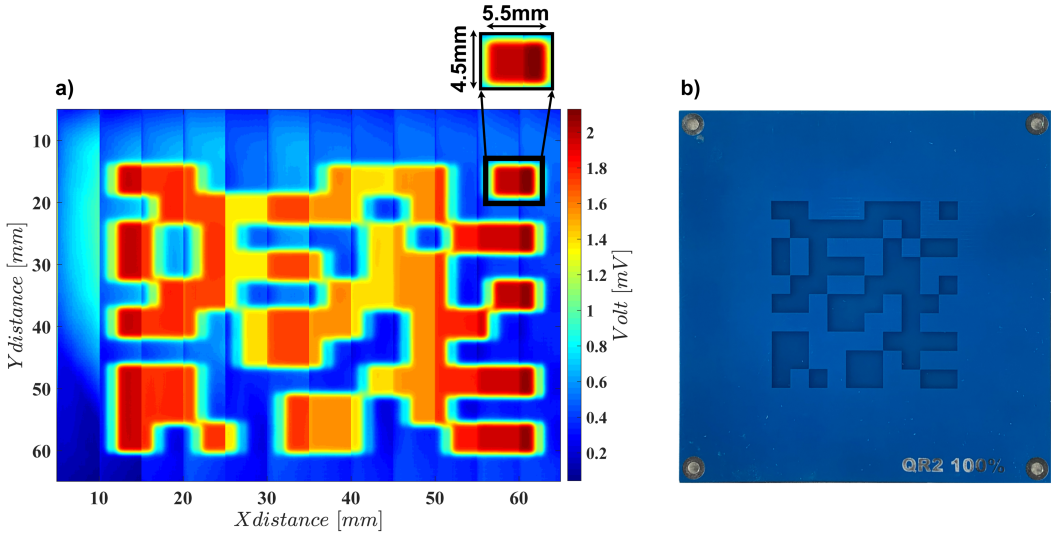

Figure 4.17: a) Bigger QR code 2D imaging and b) Scanned QR code pattern.

A fourth pattern with the same squared QR code but half of the size was analyzed to check if the probe could still detect the small patterns with a size of 2.5mm. In Fig. 4.18 a) and b) is shown the respective 2D imaging and the material under test. The test shows that the scanned patterns still have a good resolution and have almost the same size as the analyzed material. One thing noticed was that the small metal layers, between patterns, are still even less noted than in the previous scan. This was

expected because the magnetic field generated by the coils generates small eddy currents on the metal, which creates a small magnetic field detected by the measurement coil. So the smaller metal zones are less darker, making the small metal zones less visible on the 2d imaging.

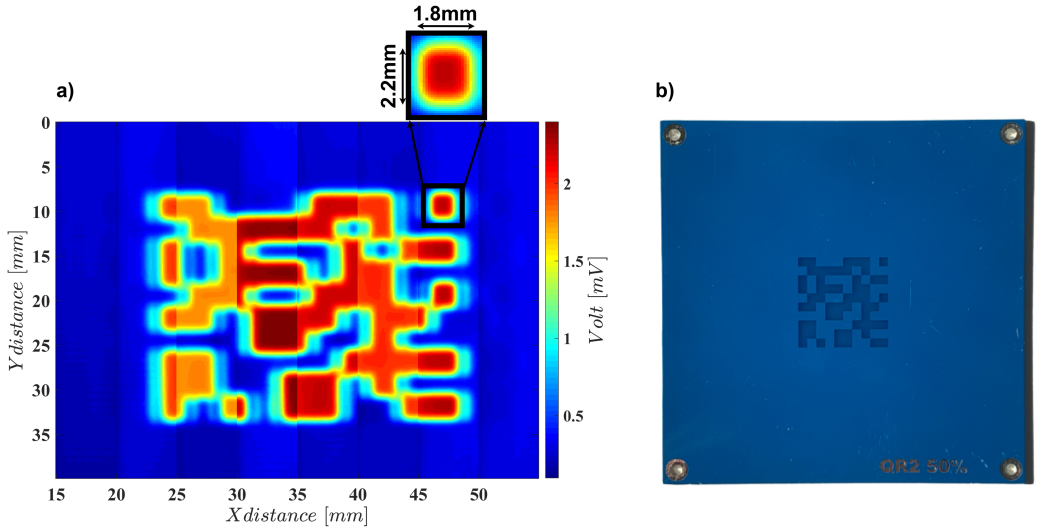

Figure 4.18: a) Smaller QR code 2D imaging and b) Scanned QR code pattern.

The final test was made in an even smaller defect. This time the defect was a hole with a 0.8mm diameter. In Fig. 4.19 a) is shown the 2D imaging of the hole and in In Fig. 4.19 b) the respective hole.

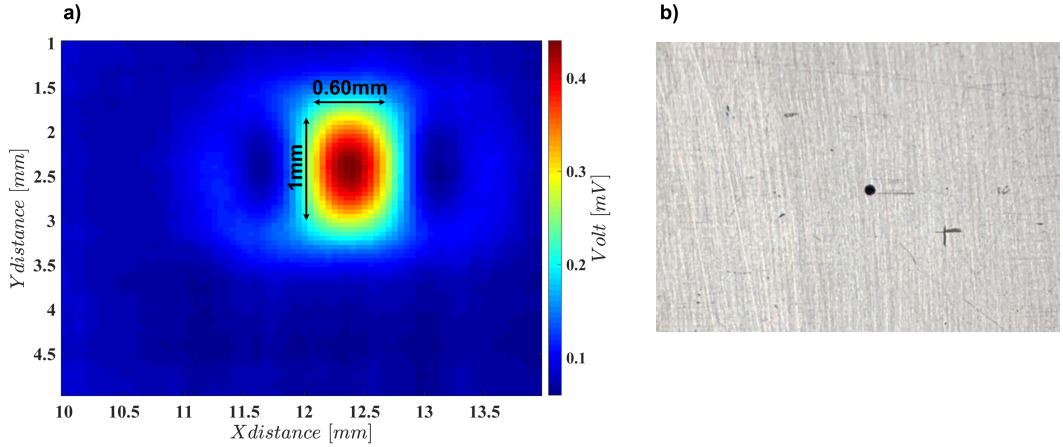

Figure 4.19: a) Hole defect 2D imaging and b) Scanned hole defect.

From the 2D imaging, it can be observed that the error is more significant compared to other bigger analyzed defects. However, the approximation distances obtained are still a good approximation.

5

Conclusions

This project presents a system based on a ECT method for the QC of the in-situ monitoring, layer by layer, of manufactured pieces using PBF technology, which is a manufacturing process on the MAM industry. Nowadays, this type of technology is used even more to create a final product, and so in order for this technology to gain mass adoption, it is essential to have high QC standards.

Therefore, in this project, the first objective was to develop an array probe based on eddy currents to assure the QC of produced PBF parts. Another objective was to make a probe scalable in terms of area and cost. For this project, a CNC machine was used to replicate a PBF machine, and some patterns were analyzed as if they were an actual layer made by the PBF machine.

Initially, in the project, some coils were tested in order to decide which were the best sensing elements for the final array probe. After that, some PCBs were developed in order to reduce as much hardware as possible and optimize the costs per channel for the final array probe. In the end, the developed array probe has sixteen channels for stimulation and reading and a size of 8x8cm, which means the final array probe can analyze materials in one sweep of 8 cm and all of that with a minimal cost of 40€. In theory, if the user would like to have a more extensive coverage area, it would only need to put probes side by side, and if it would want to increase the resolution per sweep, it would only have to put the PCBs interleaved.

In the end, the results were the expected. The array probe scanned different types of patterns and defects of a size as small as 0.8mm. The worst part was the time that the CNC machine would take to scan a pattern. The biggest pattern with a size of 8x8cm with a step of 0.1mm would take almost three hours to be thoroughly scanned. So due to that, the future work suggestions are focused on improving faster readouts from the sensors and improving the array probe's accuracy and are as follows.

- Make a control system that can move the CNC machine and acquire data at the same time in order to have a faster system;
- Evaluate different algorithms for the inspected surface reconstruction from the probe provided data. Specifically, the use of Deep-Learning may provide interesting results while dealing with the complex relation between the surface features and the ECT imaging data;
- Ensure the necessary high-level synchronization with other probe modules, for instance, providing an input for a higher level clock instance;
- Define and implement a faster digital readout architecture for several microcontroller instances. For example, using a Field Programmable Gate Array (FPGA) to aggregate and dispatch through USB the output data from multiple microcontrollers connected through a Serial Peripheral Interface (SPI) bus;
- Evaluate other eddy current sensing strategies as the use of commercial magneto-resistive sensors as the Crocus Technology CT-100;

- Evaluate the probe on real PBF produced parts and specifically during the processing of the successive layers.

Bibliography

[1] F. H. Kim, S. P. Moylan, "Literature Review of Metal Additive Manufacturing Defects", Advanced Manufacturing Series (NIST AMS), 2018.

[2] R. Abrantes, "Electronic System for Non-Destructive Testing using Eddy Currents Array Probes," Master's thesis, Instituto Superior Técnico, May 2014.

[3] N. Rodrigues, "A portable embedded contactless system for the measurement of metallic material conductivity and lift-off," Master's thesis, Instituto Superior Técnico, December 2017.

[4] Depth of Penetration and Current Density. [Online]. Available: https://www.nde-ed.org/EducationResources/CommunityCollege/EddyCurrents/Physics/depthcurrentdensity.htm

[5] Display - Complex Impedance Plane (eddy scope). [Online]. Available: https://www.nde-ed.org/EducationResources/CommunityCollege/EddyCurrents/Instrumentation/impedanceplane.htm

[6] Eddy Current Probe Selection Information. [Online]. Available: https://www.olympus-ims.com/en/ec-probes/selection/

[7] A. Silvestre, "IoT ready Eddy Current Testing Structural Health Monitor," Master's thesis, Instituto Superior Técnico, October 2019.

[8] Eddy Current Weld Inspection. [Online]. Available: http://www.vnsndt.com/services/3

[9] Fastener Hole Inspection with Eddy Current without Filter Adjustment. [Online]. Available: https://www.olympus-ims.com/pt/applications/fastener-hole-inspection-with-eddy-current-without-filter-adjustment/

[10] What is Eddy Current Testing? [Online]. Available: http://www.wermac.org/others/ndt_eddy_current.html

[11] Probes - Configurations. [Online]. Available: https://www.nde-ed.org/EducationResources/CommunityCollege/EddyCurrents/ProbesCoilDesign/ProbesConfig.htm

[12] Flexible Eddy Current Array Probe. [Online]. Available: http://tawada-ndt.com/ndt/product/non-destructive-testing/eddy-current-array/flexible-eddy-current-array-probe/

[13] 3D Printing. [Online]. Available: http://www.custompartnet.com/wu/3d-printing

[14] Sheet Lamination. [Online]. Available: https://engineeringproductdesign.com/knowledge-base/sheet-lamination/

[15] Advantages of Wire AM vs. Powder AM. [Online]. Available: http://www.sciaky.com/additive-manufacturing/wire-am-vs-powder-am

[16] Direct Metal Laser Sintering. [Online]. Available: http://www.arcam.com/technology/electron-beam-melting/hardware/

[17] S. Clijsters, T. Craeghs, S. Buls, K. Kempen, J.P. Kruth, "In situ quality control of the selective laser melting processusing a high-speed, real-time melt pool monitoring system", Int J Adv Manuf Technol, vol. 75, pp. 1089-1101, 2014.

[18] Eddy-current testing. [Online]. Available: https://en.wikipedia.org/wiki/Eddy-current_testing

[19] Ampere-Maxwell. [Online]. Available: https://em.geosci.xyz/content/maxwell1_fundamentals/formative_laws/ampere_maxwell.html/

[20] Faraday's law of induction. [Online]. Available: https://en.wikipedia.org/wiki/Faraday's_law_of_induction

[21] Z.Mottl, "The quantitative relations between true and standard depth of penetration for air-cored probe coils in eddy current testing", NDT International, vol. 23, pp. 11-18, 1990.

[22] L. Rosado, "New Non-Destructive Test Technique on Metal inspection," Master's thesis, Instituto Superior Técnico, November 2009.

[23] Probes - Mode of Operation. [Online]. Available: https://www.nde-ed.org/EducationResources/CommunityCollege/EddyCurrents/ProbesCoilDesign/ProbesModeOp.htm

[24] Eddy Current Array Tutorial. [Online]. Available: https://www.olympus-ims.com/en/ndt-tutorials/eca-tutorial/

[25] L. Rosado, "Non-Destructive Testing Based on Eddy Currents," Ph.D. dissertation, Instituto Superior Técnico, December 2014.

[26] W. Yin, S. J. Dickinson, A. J. Peyton, "A multi-frequency impedance analysing instrument for eddy current testing", Measurement Science and Technology, vol. 17, pp. 393-402, 2006.

[27] R. Grossinger, M. Kupferlinga, P. Kasperkovitz, ”Eddy currents in pulsed field measurements”, J. Magn. Magn. Mater, vol. 242, pp. 911-914, 2002.

[28] L. Shu, H. Songling, Z. Wei, Y. Peng, ”Study of pulse eddy current probes detecting cracks extending in all directions”, Sensors and Actuators, vol. 141, pp. 13-19, 2008.

[29] N.J.R. Venekamp, H. Lefever, ”Application Areas of Additive Manufacturing : From Curiosity to Application”, IEEE Technology and Society Magazine, vol. 34, pp. 81-87, 2015.

[30] W. J. Sames, F. A. List, S. Pannala, R. R. Dehoff, S. S. Babu, ”The metallurgy and processing science of metal additive manufacturing”, International Materials Reviews, vol. 61, pp. 315-360, 2016.

[31] J. Bento, “Non-Destructive Testing of large metal parts produced by Wire Arc Additive Manufacturing,” Master’s thesis, Instituto Superior Técnico, June 2018.

[32] M. Grasso, B. Colosimo, ”Process defects and in situ monitoring methods in metal powder bed fusion: a review”, Measurement Science and Technology, vol. 28, n. 4, 2017.

[33] F. Calignano, M. Galati, L. Iuliano, ”A Metal Powder Bed Fusion Process in Industry: Qualification Considerations”, Machines, vol. 7, n. 72, 2019.

[34] T. Fleming, S. Nestor, T. Allen, M. Boukhaled, N. Smith, J. Fraser, “Tracking and controlling the morphology evolution of 3D powder-bed fusion in situ using inline coherent imaging”,Additive Manufacturing, vol. 32, 2020.

[35] J. Bartlett, F. Heim, Y. Murty, X. Li, ”In situ defect detection in selective laser melting via full-field infrared thermography”, Additive Manufacturing”, vol. 24, pp. 595-605, 2018.

[36] R. Smith, M. Hirsch, R. Patel, W. Li, A. Clare, S. Sharples, ”Spatially resolved acoustic spectroscopy for selective laser melting”, Journal of Materials Processing Technology, vol. 236, pp. 93-102, 2016.

[37] D. Pieris, T. Stratoudaki, Y. Javadi, P. Lukacs, S. Catchpole-Smith, P. Wilcox, A. Clare, M. Clark, ”Laser Induced Phased Arrays (LIPA) to detect nested features in additively manufactured components”, Materials and Design, vol. 187, 2020.

[38] J. Martín, J. Gómez-Gil, E. Vázquez-Sánchez, ”Non-Destructive Techniques Based on Eddy Current Testing”, Sensors, vol. 11, pp. 2525-2565, 2011.

[39] M. Machado, K. Antin, L. Rosado, P. Vilaça, T. Santos, “Contactless High-Speed Eddy Current Inspection of Unidirectional Carbon Fiber Reinforced Polymer”, Composites Part B, vol. 168, pp. 226-235, 2018.

[40] E. Todorov, P. Boulware, K. Gaah, ”Demonstration of array eddy current technology for real-time monitoring of laser powder bed fusion additive manufacturing process”, Proceedings of the Nondestructive Characterization and Monitoring of Advanced Materials, Aerospace, Civil Infrastructure, and Transportation Conference XII, 2018.

[41] L. Rosado, F. Cardoso, S. Cardoso, P. Ramos, P. Freitas, M. Piedade, “Eddy currents testing probe with magneto-resistive sensors and differential measurement”, Sensors and Actuators A, vol. 212, pp. 58-67, 2014.

[42] H. Ehlers, M. Pelkner, R. Thewes, “Heterodyne Eddy Current Testing using Magnetoresistive Sensors for Additive Manufacturing Purposes”, IEEE Sensors Journal, vol. 20, no. 11, pp. 5793-5800, 2020.

[43] L. Pedersen, K. Magnusson, Y. Zhengsheng, ”Eddy current testing of thin layers using co-planar coils”, Res. Nondestruct., vol. 12, pp. 53-64, 2000.

[44] D. Mercier, J. Lesage, X. Decoopman, D. Chicot, ”Eddy currents and hardness testing for evaluation of steel decarburizing”, NDT E Int, vol. 39, pp. 652-660, 2006.

[45] G. Tian,Z. Zhao, R. Baines, ”The research of inhomogeneity in eddy current sensors”, Sens. Actuat., vol. 69, pp. 148-151, 1998.

[46] M. Machado, K. Antin, L. Rosado, P. Vilaça, T. Santos, ”Contactless high-speed eddy current inspection of unidirectional carbon fiber reinforced polymer”, Composites Part B: Engineering, vol. 168, pp. 226-235, 2019.

6

Appendix A

6.1 2D Imaging of an infinite failure

This section presents the 2D imaging of an infinite failure for the 100 μH and 47 μH coils shield and non-shielded, and respective real and imaginary components.

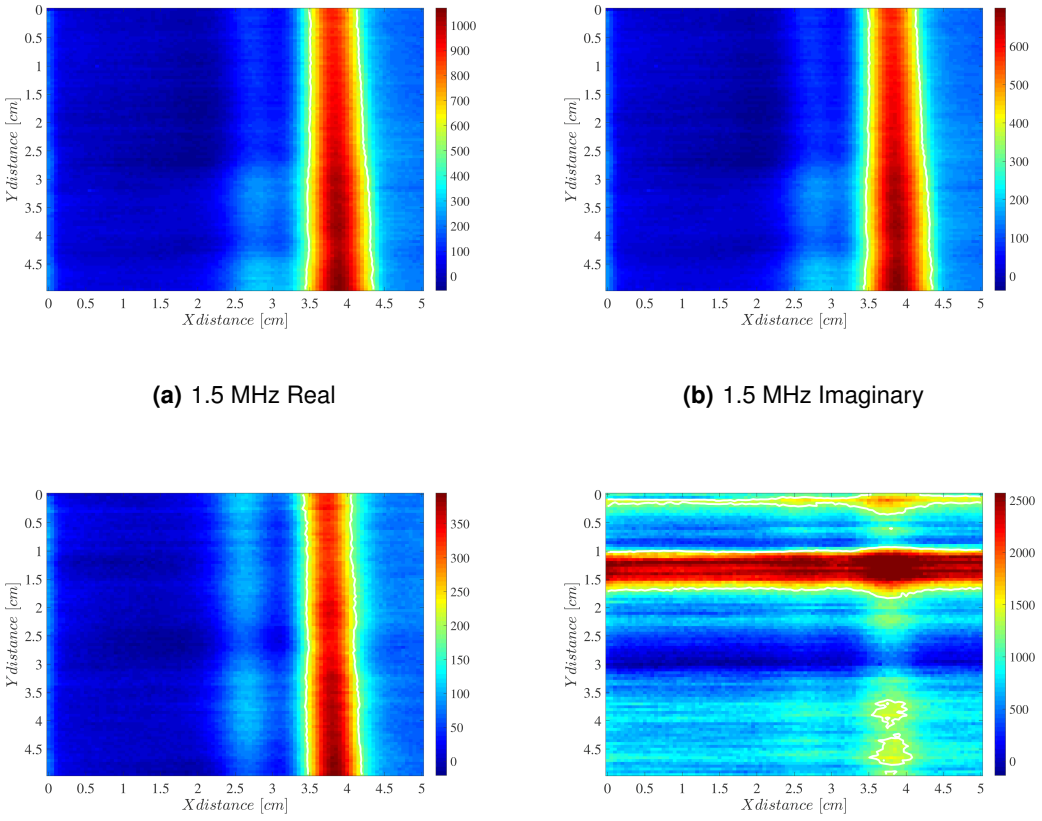

(a) 1.5 MHz Real

(b) 1.5 MHz Imaginary

(c) 1 MHz Real

(d) 1 MHz Imaginary

Figure 6.1: Infinite failure 2D imaging for a 100 μH not shielded coil

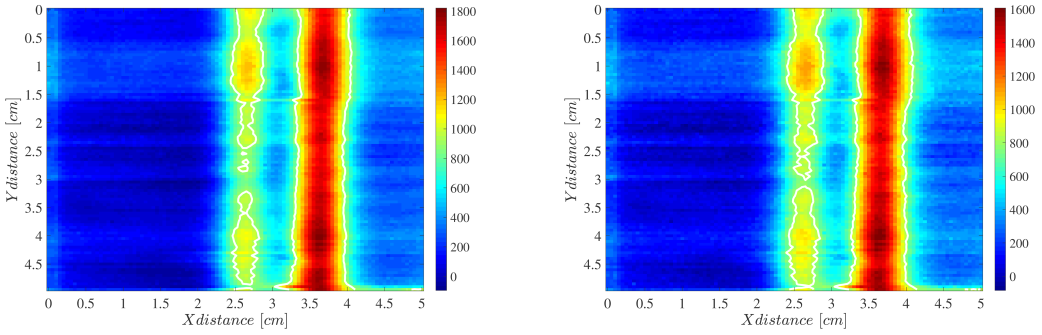

(a) 1.5 MHz Real

(b) 1.5 MHz Imaginary

(c) 1 MHz Real

(d) 1 MHz Imaginary

Figure 6.2: Infinite failure 2D imaging for a 100 μH shielded coil

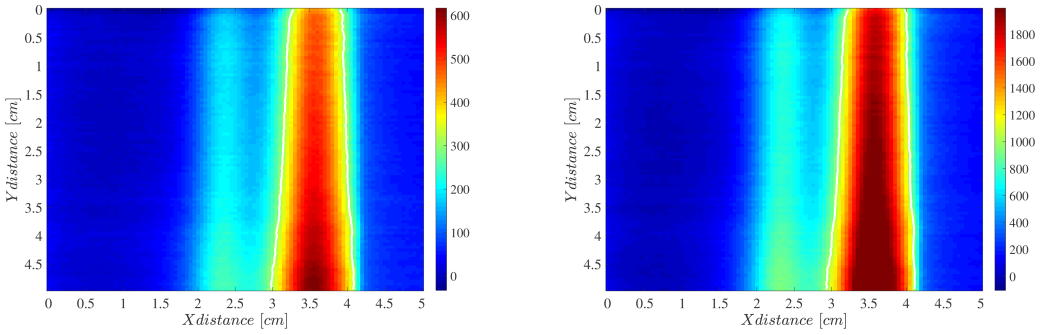

(a) 1.5 MHz Real

(b) 1.5 MHz Imaginary

(c) 1 MHz Real

(d) 1 MHz Imaginary

Figure 6.3: Infinite failure 2D imaging for a 47 μH not shielded coil

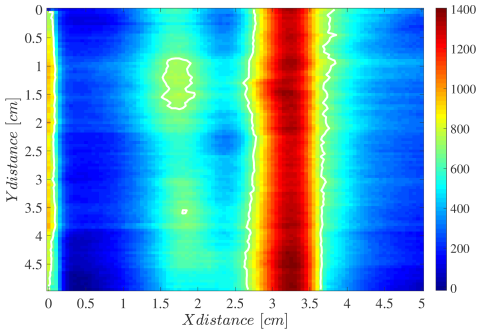

(a) 1.5 MHz Real

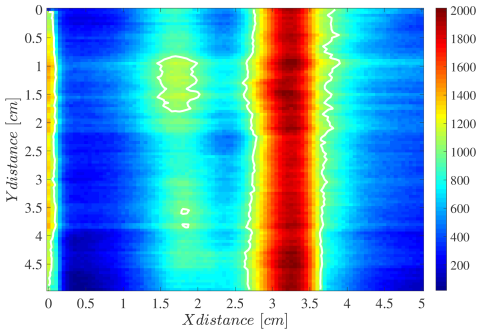

(b) 1.5 MHz Imaginary

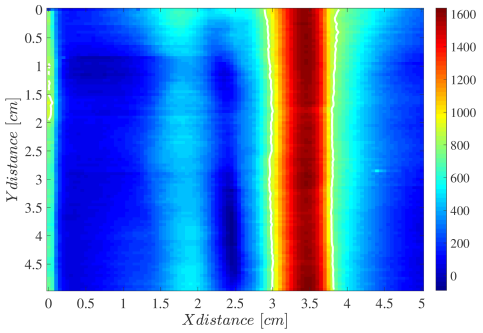

(c) 1 MHz Real

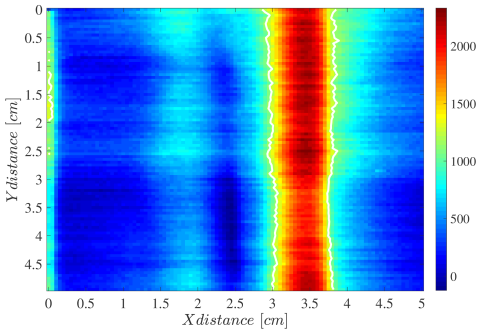

(d) 1 MHz Imaginary

Figure 6.4: Infinite failure 2D imaging for a 47 μH shielded coil

6.2 2D Imaging of the circular hole for 1.5MHz frequency

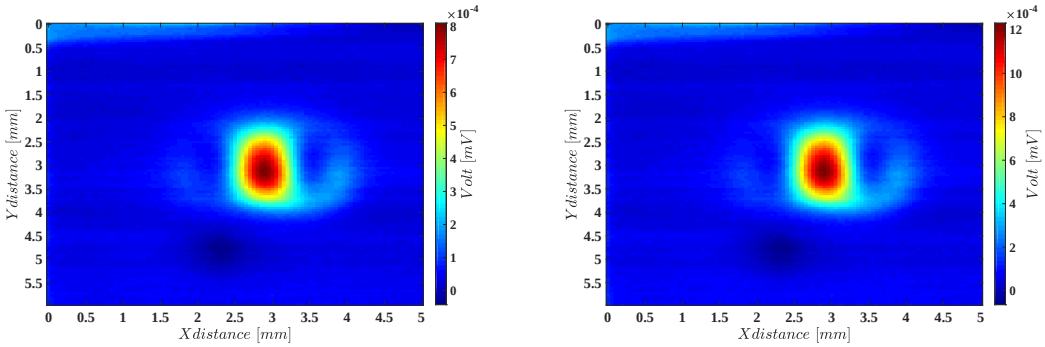

(a) 1.5 MHz Real **(b)** 1.5 MHz Imaginary

Figure 6.5: 2D imaging for a circular hole for a 100 μH non-shielded coil and 1.5 MHz stimulation.

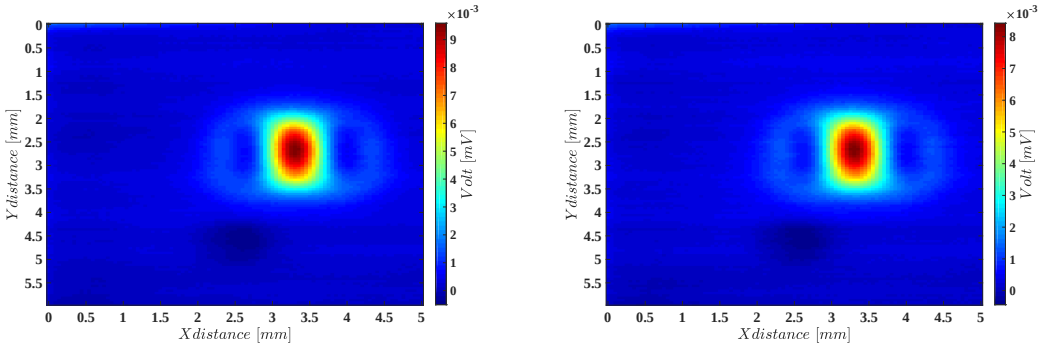

(a) 1.5 MHz Real **(b)** 1.5 MHz Imaginary

Figure 6.6: 2D imaging for a circular hole for a 100 μH shielded coil and 1.5 MHz stimulation.

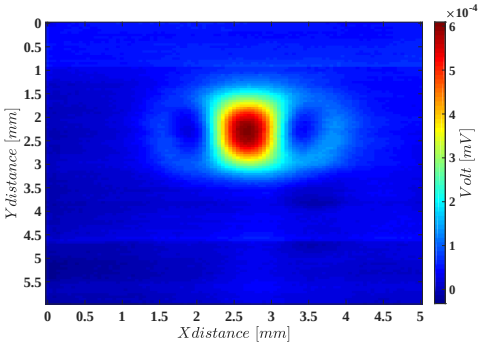

(a) 1.5 MHz Real

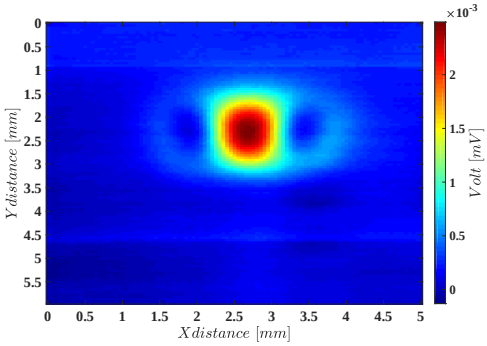

(b) 1.5 MHz Imaginary

Figure 6.7: 2D imaging for a circular hole for a 47 μH non-shielded coil and 1.5 MHz stimulation.

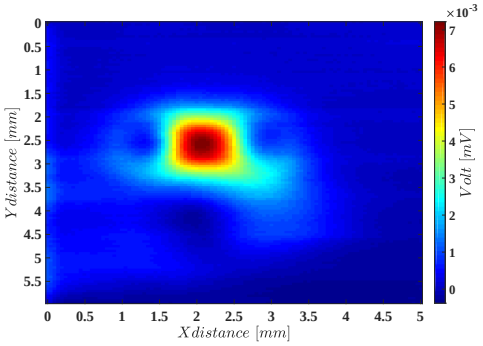

(a) 1.5 MHz Real

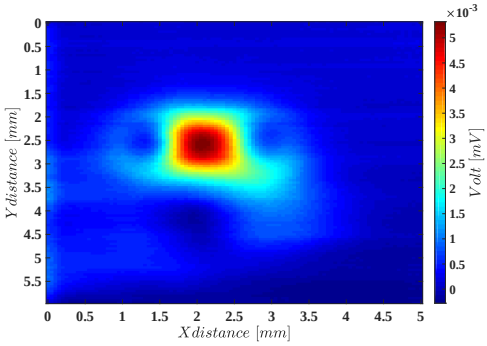

(b) 1.5 MHz Imaginary

Figure 6.8: 2D imaging for a circular hole for a 47 μH shielded coil and 1.5 MHz stimulation.